

Predictability and Dynamics of Tropical Cyclone Rapid Intensification Deduced from High-Resolution Stochastic Ensembles

FALKO JUDT^a AND SHUYI S. CHEN

Rosenstiel School of Marine and Atmospheric Science, University of Miami, Miami, Florida

(Manuscript received 1 December 2015, in final form 15 August 2016)

ABSTRACT

Rapid intensification (RI) of tropical cyclones (TCs) remains one of the most challenging issues in TC prediction. This study investigates the predictability of RI, the uncertainty in predicting RI timing, and the dynamical processes associated with RI. To address the question of environmental versus internal control of RI, five high-resolution ensembles of Hurricane Earl (2010) were generated with scale-dependent stochastic perturbations from synoptic to convective scales. Although most members undergo RI and intensify into major hurricanes, the timing of RI is highly uncertain. While environmental conditions including SST control the maximum TC intensity and the likelihood of RI during the TC lifetime, both environmental and internal factors contribute to uncertainty in RI timing. Complex interactions among environmental vertical wind shear, the mean vortex, and internal convective processes govern the TC intensification process and lead to diverse pathways to maturity. Although the likelihood of Earl undergoing RI seems to be predictable, the exact timing of RI has a stochastic component and low predictability.

Despite RI timing uncertainty, two dominant modes of RI emerged. One group of members undergoes RI early in the storm life cycle; the other one later. In the early RI cases, a rapidly contracting radius of maximum wind accompanies the development of the eyewall during RI. The late RI cases have a well-developed eyewall prior to RI, while an upper-level warm core forms during the RI process. These differences indicate that RI is associated with distinct physical processes during particular stages of the TC life cycle.

1. Introduction

Tropical cyclones (TCs) often undergo periods of rapid intensification (RI). Despite recent advancements in TC prediction, accurate forecasts of RI, which is typically defined as a ≥ 30 kt (15 m s^{-1}) increase in the maximum surface wind speed over a 24-h period (Kaplan and DeMaria 2003), remain a major challenge (Cangialosi and Franklin 2014). Because of the hazards posed by rapidly intensifying TCs and the continued difficulties in RI prediction, the RI problem is often regarded as the “holy grail” in TC intensity forecasting. It is generally accepted that RI has low predictability (for reasons that are not fully understood), but this predictability has not been precisely quantified.

While the maximum intensity of long-lasting TCs is mostly controlled by environmental thermodynamic conditions (e.g., Emanuel 1986; Emanuel 1988; DeMaria and Kaplan 1994), TC intensification is governed by complex physical and dynamical processes. Previous studies broadly agree that RI is affected by multiscale interactions between the TC environment, the mean TC vortex, and internal convective processes (e.g., Rogers 2010; Guimond et al. 2010; Rogers et al. 2015). The question of whether RI is controlled to a greater extent by environmental or internal processes is currently an area of active research with far-reaching implications for RI predictability. For instance, a recent TC predictability study showed that the mean TC vortex and the wavenumber 1 asymmetry, which are predominantly controlled by the TC environment, are predictable for much longer (>7 days) than small-scale structures, which are controlled by internal convective processes with predictability limits of <12 h (Judt et al. 2016, hereafter JCB16). JCB16 also found that the highest forecast uncertainty occurs during RI.

Focusing on the environmental influence on TC intensification, Kaplan and DeMaria (2003) and Kaplan

^a Current affiliation: National Center for Atmospheric Research, Boulder, Colorado.

Corresponding author address: Dr. Falko Judt, National Center for Atmospheric Research, P.O. Box 3000, Boulder, CO 80307.
E-mail: fjudt@ucar.edu

et al. (2010) showed that RI is more likely to occur when the TC environment is generally conducive for TC intensification (e.g., low vertical wind shear, weak upper-level forcing from troughs or cold lows, high humidity, and a warm upper ocean). However, RI has also been observed in TCs under relatively strong vertical wind shear conditions (e.g., Nguyen and Molinari 2012; Rogers et al. 2015), as well as in storms that interact with upper-level troughs (Bosart et al. 2000; Shieh et al. 2013). While the TC environment plays ostensibly an important role in RI, environmental factors alone are not able to explain 1) the abrupt nature of RI onset and 2) why some storms undergo RI whereas others intensify more gradually in similar environments (Hendricks et al. 2010).

Earlier theoretical and idealized modeling studies highlighted the importance of cooperative interactions between diabatic heating and the axisymmetric, balanced vortex-scale circulation for TC intensification (e.g., Ooyama 1969, 1982; Shapiro and Willoughby 1982). More recently, others hypothesized that the unbalanced boundary layer inflow is critical for TC spinup (e.g., Bui et al. 2009; Smith et al. 2009). The boundary inflow is in turn modulated by air–sea interactions including the TC-induced cold wake and asymmetries in the surface wave field (Lee and Chen 2012; Chen et al. 2013). All of these studies generally agree that the key dynamical process is the inward advection of angular momentum, which leads to an intensification of the swirling flow (“ice skater effect”).

The abrupt onset of RI can be explained by means of a drastic increase in thermodynamic efficiency when the heating is concentrated in a region of high inertial stability (Schubert and Hack 1982; Vigh and Schubert 2009; Nolan et al. 2007; Pendergrass and Willoughby 2009). The relationship between high inertial stability and TC intensification was confirmed by aircraft observations and full-physics modeling studies (e.g., Kossin and Eastin 2001; Rogers et al. 2013). In polar coordinates, inertial stability can be expressed as

$$I^2 = \left(f + \frac{v}{r} + \frac{\partial v}{\partial r} \right) \left(f + \frac{2v}{r} \right),$$

where r is the radial distance from the center, v the tangential wind, and f the Coriolis parameter. In TCs, the $\partial v/\partial r$ term is typically the dominant term in the inner core, where inertial stability is maximum. More specifically, the highest values of inertial stability in intensifying TCs are often found along the inner edge of the radius of maximum wind (RMW), where the magnitude of inertial stability can be $O(10^{-2})\text{ s}^{-2}$. Everything else being equal, the radial location of convective heating in

relation to the RMW is therefore important with respect to the question of whether a TC will intensify or not (Vigh and Schubert 2009; Rogers et al. 2013).

Some studies have suggested that convective processes are critical for RI initiation. In particular, intense convective features commonly referred to as convective bursts (CBs) have been hypothesized to be related to RI initiation (e.g., Hendricks et al. 2004; Reasor et al. 2009). However, satellite observations and model studies have not confirmed that CBs are either a necessary or a sufficient condition for RI (Rogers 2010; Jiang 2012). Kieper and Jiang (2012) compiled a large number of microwave satellite images and found that RI is often preceded by the development of a symmetric ring of precipitation. Nevertheless, recent investigations of Hurricane Earl (2010) showed that RI also occurs in TCs with highly asymmetric convection (Stevenson et al. 2014; Rogers et al. 2015; Chen and Gopalakrishnan 2015).

More recently, modeling studies claimed that there is a link between RI and the development of the upper-level warm core (Zhang and Chen 2012; Chen and Zhang 2013; Chen and Gopalakrishnan 2015). These case studies conclude that the pressure fall during RI is due to the hydrostatic effects of the warm anomaly in the eye. However, the question of whether the temperature anomaly is causing RI or is merely a response to the strengthening storm has not been answered yet.

In summary, RI can be regarded as a self-amplifying intensification process involving complex multiscale interactions. RI is difficult to predict, but the reasons for low RI predictability have not been fully understood. Using idealized models with prescribed environmental shear profiles, Zhang and Tao (2013) and Tao and Zhang (2014) investigated the role of wind shear in TC intensification uncertainty, and found that stronger shear leads to increased uncertainty in RI timing. Nevertheless, they could not examine the effects of environmental conditions that vary in space and time. A recent study by Judt and Chen (2015) showed that a realistic ensemble forecast of Hurricane Earl (2010) suffered from a loss of predictive skill during Earl’s RI. RI predictability may be intrinsically limited if it is dominated by convective processes (Zhang and Sippel 2009); on the other hand, RI predictability would be greater if RI is controlled by the TC environment or mean vortex properties (JCB16).

The main goal of this study is to better understand RI predictability and the physical processes associated with RI and RI uncertainty. To address these issues, we use five high-resolution stochastic ensembles of Hurricane Earl (2010) with a combined total of 100 members. Although the upper ocean and air–sea coupling are known

TABLE 1. List of SKEBS ensemble experiments.

	SKEBS-syno-PertBdy	SKEBS-syno	SKEBS_meso	SKEBS_conv	SKEBS-allScales
Perturbation scale (km)	500–4200	500–4200	24–500	2.67–12	24–4200
Domains perturbed	1–2–3	1–2–3	1–2–3	3	1–2–3
Perturbed lateral boundaries	Yes	No	No	No	No

to affect the TC intensification rate (e.g., [Hong et al. 2000](#); [Chen et al. 2013](#); [Lee and Chen 2012](#)), this study focuses only on the atmospheric properties using an uncoupled atmospheric model. In [section 2](#), we briefly review the stochastic ensembles used in [JCB16](#). Ensemble predictions of RI and their general properties are presented in [section 3](#), while RI predictability and uncertainty in RI timing are further investigated in [section 4](#). [Section 5](#) explores the question of environmental versus internal control of RI timing uncertainty, and [section 6](#) investigates the TC–environment interactions responsible for RI uncertainty. Finally, we will present two distinct dynamical modes of RI in [section 7](#) and an overall summary and conclusions in [section 8](#).

2. Stochastic ensembles

This study uses five cloud-permitting stochastic ensembles of Hurricane Earl (2010), which is one of the best-observed hurricane RI cases ([Rogers et al. 2015](#)). A short description of the ensembles follows below, and the reader is referred to sections 2a–c in [JCB16](#) for a more detailed description of the model, the ensemble method, and the experiment setup.

The ensembles, based on version 3.4 of the Advanced Research version of the Weather Research and Forecasting (WRF) Model ([Skamarock et al. 2008](#)), were generated with a stochastic kinetic energy backscatter scheme (SKEBS; [Shutts 2005](#); [Berner et al. 2009, 2011](#)). SKEBS perturbs the model fields by adding random, small-amplitude perturbations to the horizontal wind and potential temperature tendency equations at each time step. The model was set up with a stationary outer model domain covering most of the North Atlantic ($\Delta x = 12$ km), and two vortex-following domains ($\Delta x = 4$ and 1.33 km, respectively). All ensembles had 20 members, which were initialized at 0000 UTC 27 August 2010 and integrated for 7 days (168 h). Initial conditions and lateral boundary conditions were provided by the deterministic 0000 UTC 27 August 2010 Global Forecast System (GFS) forecast.

The five SKEBS ensembles differed in their perturbation characteristics ([Table 1](#)). Perturbations in the SKEBS-syno, SKEBS-meso, SKEBS-conv, and

SKEBS-allScales¹ ensembles ranged from synoptic to convective scales, spanning four orders of magnitude from $O(1000)$ km to $O(1)$ km. The perturbation-scale differences are neatly visualized in [Fig. 1](#) of [JCB16](#). In addition to perturbations within the model domains, SKEBS-syno-PertBdy featured perturbed lateral boundary conditions to simulate the uncertainty in the flow through the boundaries.

For the analyses in [sections 3, 4, and 7](#), the members of all five SKEBS ensembles were combined into one all-encompassing ensemble with 100 members, termed the SKEBS Grand Ensemble. To enable the storm-relative analysis of the physical processes and structural changes in [section 7](#), the hourly model output of all 100 members was interpolated onto a cylindrical coordinate grid with $r_{\max} = 300$ km and grid spacings of $dr = 2.0$ km, $d\theta = 1.0^\circ$, and $dz = 500$ m. At each vertical level, the cylindrical coordinate grid is centered on the local height-varying vortex center.

3. Ensemble predictions of Earl's rapid intensification

a. Hurricane Earl (2010)

Earl was a typical Cape Verde-type hurricane that formed from an African easterly wave on 24 August 2010 and recurved over the western Atlantic. During the 7-day forecast period from 0000 UTC 27 August to 0000 UTC 3 September 2010, Earl's intensity evolution followed the typical life cycle of a major hurricane, including 1) gradual intensification during the tropical storm/minimal hurricane stage, 2) RI to a major hurricane, 3) a period of relatively steady maximum intensity, and 4) the beginning of extratropical transition.

The ensemble captured Earl's track across the basin and its recurvature, but featured an eastward bias that increased over time ([Fig. 1a](#)). In general, the members were also able to predict the four main stages of Earl's intensity evolution in terms of maximum 10-m wind speed ([Fig. 1b](#)) and minimum SLP ([Fig. 1c](#)). While the

¹ The SKEBS-allScales ensemble, featuring a superposition of synoptic- and mesoscale perturbations, was not part of the original [JCB16](#) ensemble experiments.

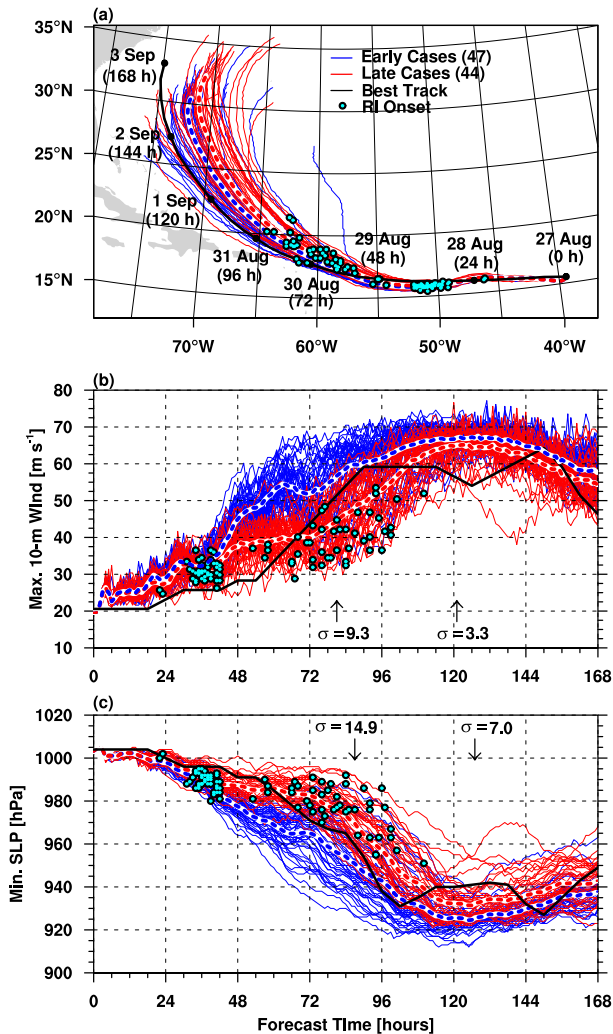


FIG. 1. (a) SKEBS Grand Ensemble track and (b),(c) intensity forecasts for Hurricane Earl (2010). Only the 91 members that qualified as RI cases are included here. Members with RI onset before $t = 48$ h (“early cases”) are in blue, and members with RI onset after $t = 48$ h (“late cases”) are in red. The cyan dots indicate the RI onset of each member, and the thick dashed lines denote the respective means of the early and late cases. The NHC best track estimates are in black. Sigma values and arrows indicate the magnitude and time of the maximum (9.3 m s^{-1} , 14.9 hPa) and minimum (3.3 m s^{-1} , 7.0 hPa) standard deviations after the intensity bifurcation, respectively.

ensemble captured the general intensity trend, most members suffered from a wind speed high bias during the early intensification period and missed the temporary weakening around $t = 120$ h.

Following the RI definition of Kaplan and DeMaria (2003), we identified ensemble members as RI cases when the maximum wind increased by at least 15 m s^{-1} within a 24-h interval. To objectively determine RI onset as the time that best corresponds to a subjective

impression of RI onset (i.e., the time when the rate of intensification begins to increase dramatically), we added the constraint that the intensification rate must be $>0.625 \text{ m s}^{-1} \text{ h}^{-1}$ [$15 \text{ m s}^{-1} (24 \text{ h})^{-1}$] during the entire 24-h window. This constraint also excludes short-lived intensity fluctuations, which are not representative of changes in the overall TC circulation. With 91 out of 100 Grand Ensemble members qualifying as RI cases, the ensemble forecasts evidently predicted favorable conditions that resulted in the vast majority of members undergoing RI during the TC’s lifetime.

b. Maximum intensity, RI, and RI timing

One of the most intriguing ensemble characteristics is the large uncertainty in terms of intensity between $t = 36$ and 120 h, encompassing Earl’s RI period (Fig. 1b). Nearly all of the uncertainty is related to RI timing differences; the time window during which RI occurs spans more than 3 days. The earliest and latest RI onsets occur at $t = 22$ and 110 h, respectively (RI onset is marked by cyan dots in Fig. 1). Ensemble standard deviations of intensity reach maxima of $\sigma_{v_{\text{max}}} = 9.3 \text{ m s}^{-1}$ at $t = 81$ h and $\sigma_{\text{MSLP}} = 14.9 \text{ hPa}$ at $t = 84$ h. To appreciate this extreme amount of intensity uncertainty, note that around $t = 72$ h the intensity of the members ranges from tropical storms to category 4 events.

The timing of RI onset is not spread out uniformly during the overall RI period, but clustered into two groups. The lack of RI onset occurrences between $t = 42$ and 53 h facilitates a separation into two groups: members with RI onset before $t = 48$ h are designated the early RI cases (blue), whereas members beginning RI after $t = 48$ h are termed late RI cases (red). The cluster composed of the early RI cases is comparatively dense, and all members are of tropical storm/minimal hurricane intensity at RI onset (maximum winds of $26\text{--}37 \text{ m s}^{-1}$). In contrast, the late cases form a more scattered cluster with a much wider range of intensities at RI onset, ranging from tropical storm to category 3 (maximum winds of $28\text{--}53 \text{ m s}^{-1}$).

Despite the differences in RI timing, eventually all 91 RI cases become major hurricanes, and the maximum wind speed uncertainty decreases by 65% to a value of $\sigma = 3.3 \text{ m s}^{-1}$ at $t = 121$ h. Similarly, the standard deviation of the minimum SLP more than halves from $\sigma = 14.9$ to 7.0 hPa at $t = 127$ h. The drastic reduction in uncertainty after the RI period suggests that RI and the maximum intensity period are governed by regimes with distinct uncertainty characteristics.

The overall difference between the two groups is highlighted by their respective means (dashed lines in Fig. 1). Before $t = 36$ h, both groups are practically indistinguishable, but afterward their evolution diverges,

and by $t = 37$ h the difference becomes statistically significant with 99% confidence. The time period around $t = 36$ h (Figs. 1b,c) marks a bifurcation point and seems to be critical in determining whether a member will undergo RI before $t = 48$ h or not. The rate of intensification increases for all members around $t = 36$ h, but the late cases cease to strengthen about 12 h into this short-lived intensification period (Fig. 1b). These members are therefore not able to meet the RI criterion (until later). The spread between the two groups increases rapidly, and at $t = 64$ h the early cases are on average 14 m s^{-1} stronger. Despite the failure to undergo RI early in the forecast, the late cases are presented with a second chance to rapidly intensify between $t = 53$ and 110 h. Yet, despite RI, the late cases remain on average $\sim 5 \text{ m s}^{-1}$ weaker during the maximum intensity period and beyond (statistically significant with 99% confidence).

4. Predictability of RI and uncertainty in RI timing

Adapting the definition of Thompson (1957), predictability of RI here refers to the extent to which it is possible to predict whether a TC will undergo RI. Given that about 90% of the 100 ensemble members predicted RI, it seems that Earl's RI was, to a certain degree, predictable (strictly speaking, we do not know whether the 90% reflects the true probability in nature, since the WRF SKEBS ensembles have not been calibrated with TC observations). However, the ensemble reveals that there is large uncertainty in RI timing, which is particularly important for operational TC forecasting. The predictability of RI can therefore be examined in terms of 1) the likelihood of RI during the TC lifetime and 2) the timing of RI. Both aspects are important, as the first provides a basic level of confidence whether a TC may become an intense storm at some point along a forecast path, while the second deals with the problem of directly forecasting TC intensity on shorter time scales. In sections 4–6, we will examine the factors that lead to Earl's RI and control the ability of the ensemble to predict RI, and investigate the processes that cause the uncertainty in RI timing.

a. Environmental factors

The SST used in the model is from the NCEP 0.5° -resolution analysis, which is relatively smooth compared with satellite observations. During the first 2–3 days of the forecast, SST increases along the ensemble storm tracks as the TCs move from the central Atlantic into a region with higher SSTs (Fig. 2). During the early RI period, all members are over warm waters of 29.0° – 29.5°C , indicating that the thermodynamic ocean environment

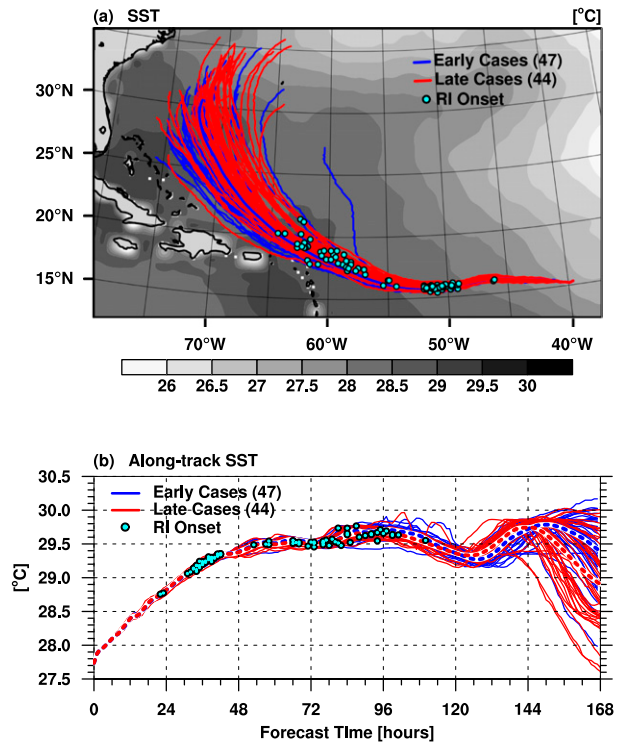


FIG. 2. (a) Model SST (in $^\circ\text{C}$) with ensemble tracks overlaid, and (b) ensemble time series of along-track SST. Early RI cases are in blue, and late cases in red. The thick dashed lines in (b) denote the respective means, and the cyan dots in (a) and (b) indicate the times of RI onset.

is conducive for intensification. SSTs are even $\sim 0.5^\circ\text{C}$ higher when the late cases begin RI 2–3 days later. After the storms have spent a few days over the warm waters of the western Atlantic, the SST decreases for the majority of the members as they recurve into the midlatitudes. Since all members have constant SST in time in the uncoupled model, differences in SST can only be associated with differences in track. During the RI period of the early cases, all ensemble tracks are tightly clustered, and the along-track SST traces show that there are practically no SST differences between the groups (Fig. 2b). Statistically significant differences in SST arise not until after the majority of the late cases had begun RI at $t = 96$ h. Evidently, differences in RI timing cannot be explained by differences in SST in these ensemble experiments. The uniformly high SST is likely one of the factors leading to Earl's RI, and one of the reasons why 90% of the ensemble members predict RI in this case.

Following Chen et al. (2006), the environmental vertical wind shear is defined as the difference between the mean wind vectors of the 200- and 850-hPa levels averaged within a 200–800-km annulus around the storm

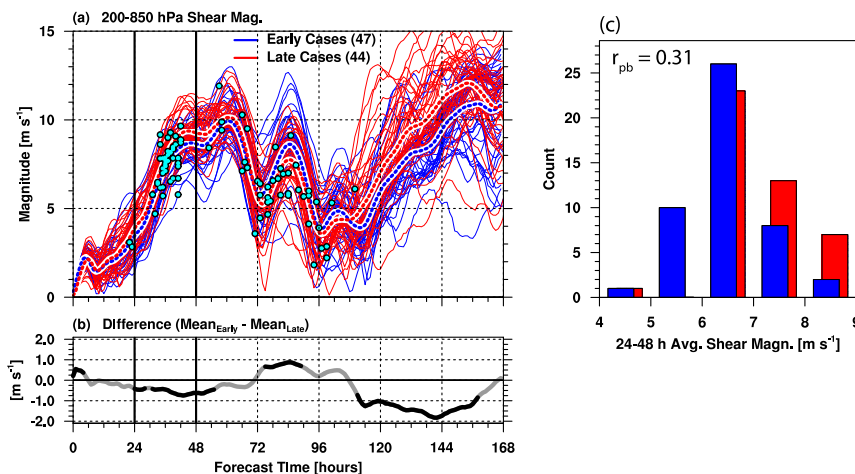


FIG. 3. (a) Ensemble time series of deep-layer vertical wind shear magnitude. Early cases are in blue, and late cases in red. The thick dashed blue (red) lines denote the means of the early (late) subsets, and the cyan dots indicate the time and shear magnitude at RI onset. (b) Difference between the mean shear of the early and late subsets, where statistical significance (95% confidence interval) is highlighted in black. (c) Histograms of shear magnitude averaged over the intensity bifurcation period between $t = 24$ and 48 h; the time window is marked by vertical black lines in (a) and (b). Early and late subsets are in blue and red, respectively. The point-biserial correlation coefficient based on the distributions in (c) is $r_{pb} = 0.31$, indicating a weak-to-moderate relationship between shear magnitude and RI onset time.

center. Forecasts of shear magnitude reveal a complex and dynamic shear pattern during the 7-day period (Fig. 3a). Broadly, there are two episodes of low shear, each followed by periods of much higher shear. Early in the forecast ($t = 0$ –18 h), shear was uniformly low ($<5 \text{ m s}^{-1}$), but it increased drastically between $t = 24$ and 48 h, reaching peak values of $>12 \text{ m s}^{-1}$ by $t = 60$ –66 h. [This increase in shear was also observed during Earl's RI (Rogers et al. 2015).] In spite of the shear increasing from ~ 5 to 10 m s^{-1} , the early cases begin the RI process. The environment was in general somewhat more hostile for the late RI cases, which featured significantly higher shear between $t = 22$ and 57 h ($p = 0.05$). The difference between the two means reached a local maximum of close to 1 m s^{-1} at $t = 42$ h (Fig. 3b).

The evolution of the shear magnitude in Fig. 3a reflects changes in the synoptic-scale environment around Earl. For example, the prominent increase in shear after $t = 12$ h was related to the upper-level outflow of Hurricane Danielle, which was located near 28°N , 62°W at $t = 24$ h (Figs. 4a,b). At this time, the shear differences between the early and late groups were just starting to become apparent, but by $t = 54$ h the contrast had become obvious (Figs. 4c,d). In agreement with Figs. 3a and 3b, the shear composite of the late cases shows a much more striking shear maximum impinging on Earl than in the early cases.

After $t = 66$ h, the storms moved away from the shear maximum, and by $t = 90$ h all members had moved into a low-shear environment (Figs. 4e,f). The decreasing

shear created a more conducive environment for intensification, within which the late cases began the RI process. We speculate that this decrease in shear is allowing the members in the late subset to undergo RI. The significant differences in shear magnitude between the two groups during the final two days of the forecast (Fig. 3a) were associated with track differences, as the late cases tended to move farther north, closer to the higher shear associated with stronger upper-level westerlies.

The statistical relationship between shear magnitude and RI timing in the Grand Ensemble is summarized in Fig. 3c, which shows that the shear (averaged from $t = 24$ to 48 h) is generally lower in the early RI cases. However, there is a considerable amount of overlap between the two groups, indicating that shear is not the only factor explaining the RI timing differences. Correlating the 24–48-h time-averaged shear magnitude with the dichotomous variable *RI onset time* (early RI = 0; late RI = 1) yields a point-biserial correlation coefficient of $r_{pb} = 0.31$, which is commonly interpreted as weak correlation.

In addition to SST and wind shear we also examined the midlevel relative humidity in the ensemble. Humidity differences in the near-storm environment between the members were $\leq 5\%$, because all members were embedded in an envelope of moist air (relative humidity $>70\%$). The lack of variability indicates that RI timing uncertainty was not related to midlevel

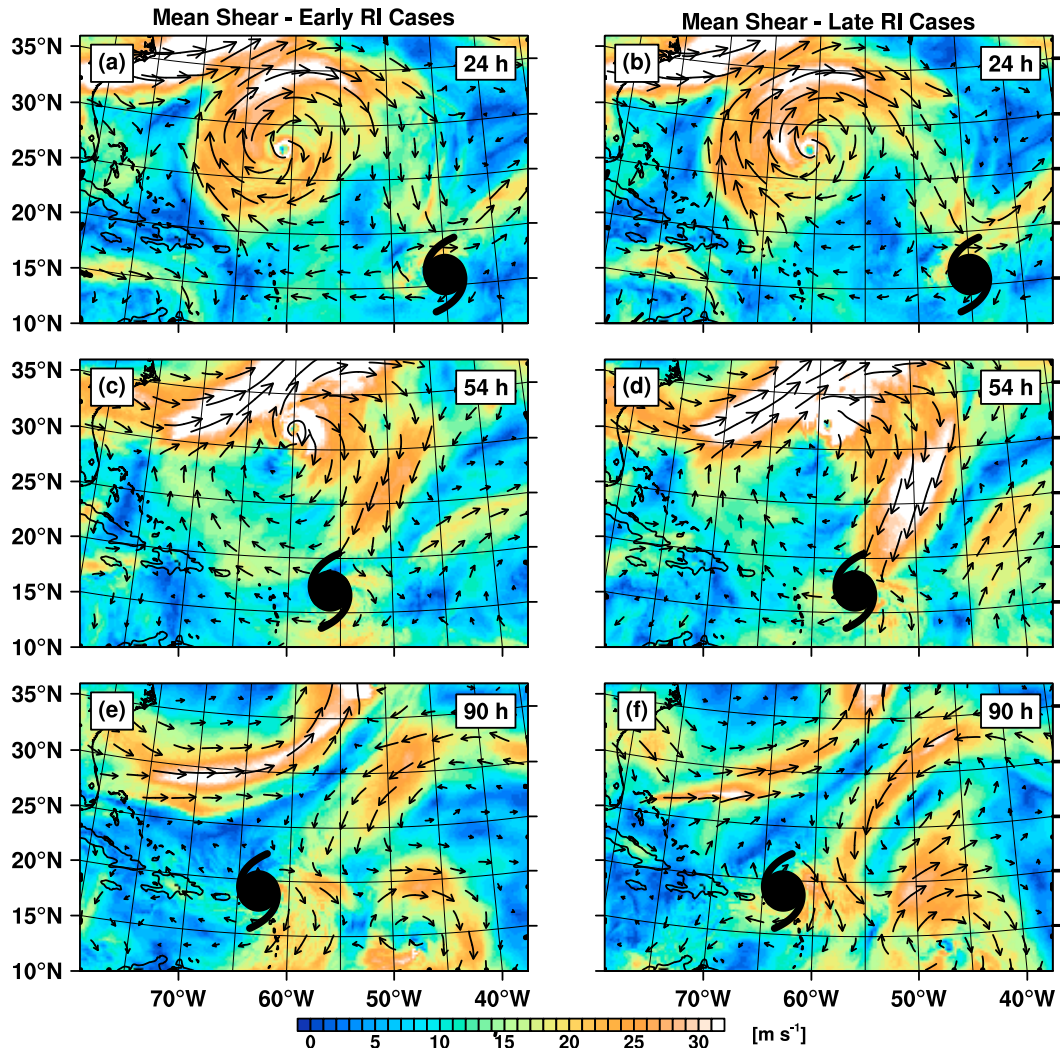


FIG. 4. Snapshots of 850–200-hPa vertical wind shear at $t =$ (a),(b) 24; (c),(d) 54; and (e),(f) 90 h. Shown are the means of the (left) early and (right) late RI subsets. The black TC symbols indicate the mean TC position during each time period.

moisture differences. Braun et al. (2013) and Rogers et al. (2015) also mentioned the envelope of low- and midlevel moisture around Earl, which shielded the TC from a dry Saharan air layer to its north and provided favorable conditions for RI.

b. Internal factors

As a first step to exploring the role of internal factors on RI timing uncertainty, we investigated the relationship between RI onset and TC intensity itself. The maximum wind speed and minimum sea level pressure begin to loosely correlate with RI timing after $t = 18$ h, or about 18 h before the intensity bifurcation (Fig. 5a). In both metrics, the correlation becomes statistically significant ($p = 0.05$) by $t = 20$ h. The correlation

between maximum wind speed and RI onset decreases shortly after $t = 24$ h, loses significance by $t = 26$ h, and the two quantities are uncorrelated by $t = 30$ h. In contrast, the weak-to-moderate correlation ($r_{pb} \sim 0.4$) between minimum SLP and RI onset endures and remains statistically significant. A more robust relationship between vortex strength and RI onset emerges when correlating the maximum azimuthally averaged tangential wind speed at each vertical level with RI onset (Fig. 5b). The correlation here also begins to show after $t = 18$ h and is comparatively stronger at the upper levels, where it reaches values of >0.5 between altitudes of 7.5 and 10 km. Tangential wind speed at higher altitudes and minimum sea level pressure are evidently much better predictors of RI onset than the maximum wind speed,

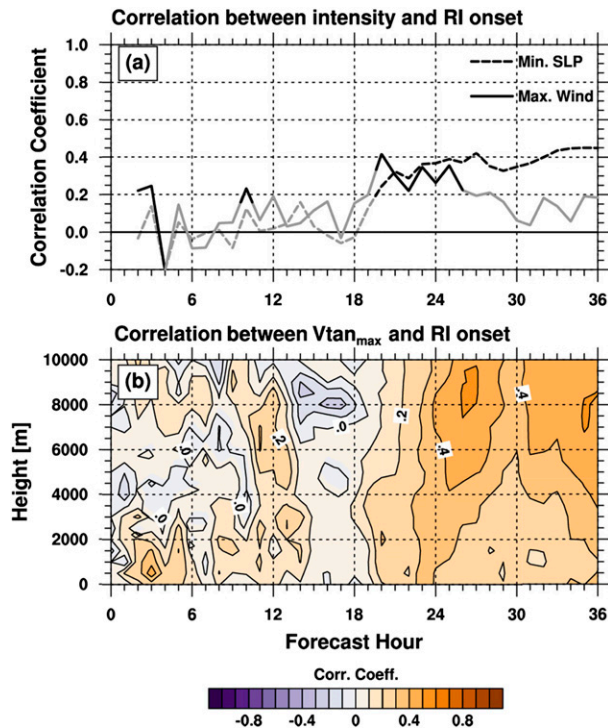


FIG. 5. (a) Correlation between intensity and RI onset, where statistical significance (95% confidence interval) is highlighted in black. (b) Correlation between the maximum azimuthally averaged tangential wind speed at each vertical level and RI onset time computed from the SKEBS Grand Ensemble.

which suggests that the vertical extent and structure of the vortex may be more important for RI than intensity itself.

The vertical TC structure is further analyzed by examining the tilt of the vortex (Fig. 6). During the first couple of hours, the magnitude of the vortex tilt, here expressed as the distance between the 2- and 6-km storm centers, decreases substantially for both early and late cases (Fig. 6a). Then, between 18 and 24 h, the tilt in the late cases increases abruptly, likely in response to the increasing shear, while the early cases continue their vertical alignment. It follows that after 18 h the early cases have a significantly smaller tilt ($p = 0.05$). The difference between the subsets reaches its maximum shortly after 24 h (Fig. 6b). At this time, about 8–12 h before the RI onset in the early cases, the average vortex tilt of the early cases is 15 km, whereas it is 30 km for the late cases. Except for the outliers that begin RI before $t = 24$ h, all early cases feature a tilt of <10 km at RI onset, while the tilt magnitudes range from 3 to 20 km when the late cases begin RI. The statistical summary in Fig. 6c reveals a moderate correlation between vortex tilt (averaged between 24 and 33 h) and RI onset time ($r_{pb} = 0.45$), indicating that the

vertical structure of the vortex is an important factor in RI. This relationship is consistent with the shear analysis in Fig. 3.

Inertial stability is a quantity that is a measure of the dynamic structure of the inner core and is often invoked in TC intensity change studies. The magnitude of the inertial stability is mostly determined by the radial derivative of the tangential wind, where a “sharper” profile corresponds to higher values of inertial stability. The time series of area-averaged ($r = 0$ –20 km) inertial stability at $z = 2$ km in Fig. 7a shows that the early cases have comparatively higher inertial stability after an abrupt increase at about $t = 18$ h (note that this is the same time when the maximum tangential wind speed starts to correlate with RI onset; see Fig. 5). The difference between the two groups becomes statistically significant ($p = 0.05$) at $t = 21$ h (Fig. 7b). Inertial stability increases at a much higher rate in the early cases during RI ($t = 36$ –48 h), and although the late cases also show an increase in inertial stability around this time, it is much smaller in amplitude and followed by decay in most cases. This decrease in inertial stability in the late cases coincides with the shear reaching its maximum (Fig. 3a), suggesting that the dynamical structure of the inner core in these members suffers from the worsening environmental conditions. The statistical relationship between inner-core inertial stability and RI timing shows a clear tendency for early RI cases to have higher inertial stability during the intensity bifurcation, or in other words, members with lower inertial stability are much less likely to undergo RI early (Fig. 7c). Similar to the relationship between shear and RI timing, there is considerable overlap between the groups, and the negative correlation between $t = 24$ –33-h time-averaged inertial stability and RI timing is moderate ($r_{pb} = -0.45$).

In addition to the dynamic quantities examined above, we will now focus on the convective characteristics in TCs. Given that CBs have been linked to RI in several previous studies (e.g., Guimond et al. 2010; Chen and Zhang 2013) and explicitly hypothesized to play a role in Earl’s RI (e.g., Chen and Gopalakrishnan 2015; Rogers et al. 2015), we examine the CB activity in the Grand Ensemble. Here, CBs are identified using the criteria put forth in Rogers et al. (2015): grid points qualify as CBs when the maximum vertical velocity in the 8–16-km layer is $>5 \text{ ms}^{-1}$ and the reflectivity averaged in the 8–14-km layer is $>20 \text{ dBZ}$. Somewhat surprisingly, there are virtually no statistically significant differences between the early and late cases in terms of CB activity (expressed as the area covered by CBs in the innermost model domain; Fig. 8). Although it is possible that an increase in CB area from 24 to 36 h is a precursor

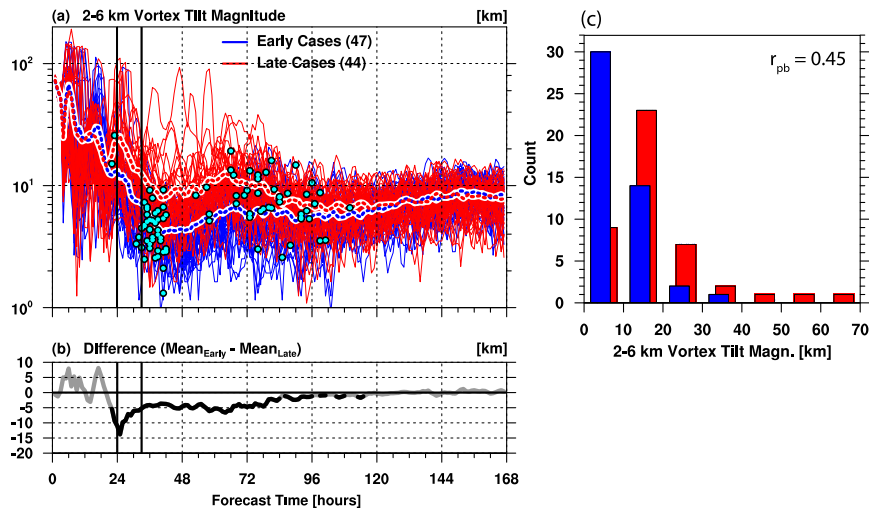


FIG. 6. (a) Ensemble time series of vortex tilt magnitude (distance between the 2- and 6-km storm centers). Early cases are in blue, and late cases in red. The thick dashed blue (red) lines denote the means of the early (late) subsets, and the cyan dots indicate the time and vortex tilt at RI onset. (b) Difference between the early and late subsets' respective mean vortex tilts, where statistical significance (95% confidence interval) is highlighted in black. (c) Histograms of vortex tilt magnitude averaged over a 9-h time window ($t = 24\text{--}33$ h) prior to the intensity bifurcation period; the time window is marked by black lines in (a) and (b). Early and late subsets are in blue and red, respectively. The point-biserial correlation coefficient based on the distributions in (c) is $r_{pb} = 0.45$, indicating a moderate relationship between vortex tilt and RI onset time.

to RI in the early cases, the lack of statistically significant differences between the groups indicates that this spike in CBs also occurred in the late RI cases without inducing RI. As a matter of fact, RI onset in the early cases occurs when the CB area reaches a distinct minimum near $t = 36$ h.

Several observational studies noted a counterclockwise azimuthal translation of CBs during Earl's evolution. Just prior to RI, CB activity propagated from the downshear-left quadrant through the upshear-left quadrant into the upshear storm sector (Stevenson et al. 2014; Rogers et al. 2015). In general agreement with these observations, the ensembles show a counterclockwise translation of CBs between $t = 26$ and 30 h, albeit with some differences between the subsets (Fig. 9). At $t = 26$ h, CB activity in the early cases is concentrated in the upshear-left quadrant (Fig. 9a). In comparison, the activity in the late cases is located in both the downshear- and upshear-left quadrants (Fig. 9b).

Four hours later, CB activity in the early cases has propagated downwind and is now located in the upshear storm sector, similar to the observations. The crescentlike azimuthal distribution of CBs is reminiscent of a developing eyewall (Fig. 9c). In contrast, CBs in the late cases are mostly confined to the upshear-left quadrant and feature a somewhat less arching pattern (Fig. 9d). The location of CBs in the early cases seems to support

one of the conjectures of Rogers et al. (2015), who hypothesize that RI occurred after vortex alignment following the upshear translation of a distinct CB.

The results in this section can be summarized as follows. The large-scale environment (SST, shear) sets the stage for Earl's RI and is likely one of the factors leading to the ability of the ensemble to predict RI (in a probabilistic sense). Both large-scale (shear) and internal (vortex tilt, inner-core inertial stability) variability are linked to RI uncertainty, but individually, they can only "explain" a relatively small amount of RI uncertainty in the SKEBS Grand Ensemble. While the maximum wind speed and RI onset time correlate only weakly, the vertical extent of stronger tangential winds seems to be a better indicator for RI onset. The moderate correlation between vortex tilt and RI onset furthermore indicates that the vertical vortex structure plays a substantial role. Differences in terms of CB activity expressed as the area covered by CBs between the two groups are not statistically significant, although the azimuthal location and interaction of CBs with the vortex seem to be important for RI.

5. Environmental and internal control of RI timing

To disentangle the effects of environmental and internal processes on RI timing, we use two ensembles

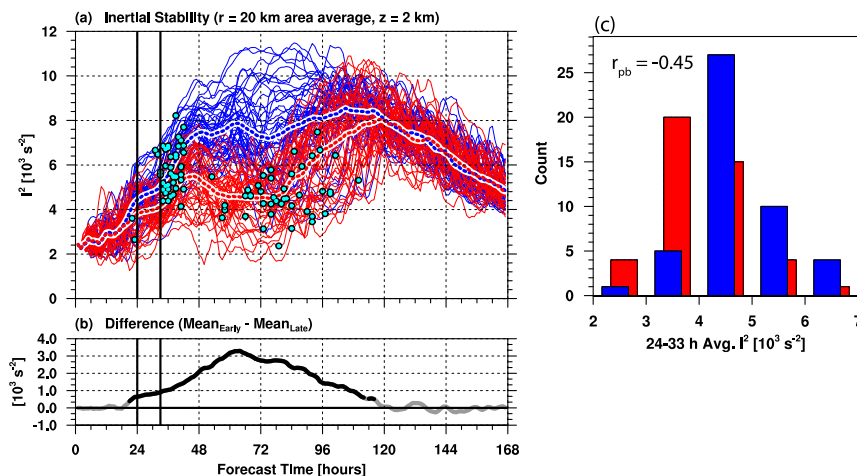


FIG. 7. (a) Ensemble time series of inertial stability, averaged over a disk with $r = 0\text{--}20$ km at $z = 2$ km. Early cases are in blue, and late cases in red. The thick dashed blue (red) lines denote the means of the early (late) subsets, and the cyan dots indicate the time and inertial stability at RI onset. (b) Difference between the early and late subsets' respective mean inertial stabilities, where statistical significance (95% confidence interval) is highlighted in black. (c) Histograms of inertial stability averaged over a 9-h time window ($t = 24\text{--}33$ h) prior to the intensity bifurcation period; the time window is marked by black lines in (a) and (b). Early and late subsets are in blue and red, respectively. The point-biserial correlation coefficient based on the distributions in (c) is $r_{pb} = -0.45$, indicating a moderate, negative relationship between inertial stability and RI onset time.

that were designed to isolate the influences of environmental and internal uncertainty on TC intensity. As described in detail in JCB16, the SKEBS-syno ensemble explicitly perturbs the wind and temperature on synoptic scales over the entire large-scale model domain, whereas the SKEBS-conv ensemble perturbs on the convective scale within the TCs in the innermost nested domain. The comparison of these two distinct ensembles can shed some light on the question of how environmental and internal processes affect RI and its timing.

a. Ensembles with synoptic- and convective-scale perturbations

In both SKEBS-syno and SKEBS-conv, 18 out of 20 members qualify as RI cases, as shown in Figs. 10a and 10b. Two members with RI onset times at opposite ends of the RI window are highlighted to contrast their disparate evolutions. Even though the intensity forecast uncertainty in SKEBS-syno is generally larger than in SKEBS-conv, there is substantial RI timing uncertainty in SKEBS-conv (earliest RI onset: $t = 22$ h; latest RI onset: $t = 97$ h). This means that RI uncertainty is not exclusively controlled by variability in the environment, and indicates that the exact timing of RI is at least partially controlled by internal variability. In contrast, the maximum intensity is much less sensitive to small-scale perturbations, and the maximum wind uncertainty in

SKEBS-conv is $\sim 40\%$ less than in SKEBS-syno during the maximum intensity period ($t = 120\text{--}144$ h).

b. Environmental wind shear variability and RI uncertainty

Wind shear time series from SKEBS-syno (Fig. 10c) and SKEBS-conv (Fig. 10d) reveal some intriguing differences between the ensembles. While there is substantial ensemble spread in SKEBS-syno, shear variability is virtually nonexistent in SKEBS-conv before $t = 48$ h because the environment is unperturbed.

Members Ens03 and Ens02 of SKEBS-syno provide an example of the relationship between RI timing and shear (Fig. 10c). Ens03, an early RI case, features 6 m s^{-1} shear at its RI onset around $t = 36$ h, whereas Ens02 has nearly twice as much shear at that time. Not surprisingly, Ens02 fails to rapidly intensify during this period, but it begins the RI process at $t = 84$ h when the shear has decreased. This straightforward relationship between lower shear and early RI does not hold in the case of the SKEBS-conv ensemble. All members are subject to the same shear magnitude during the intensity bifurcation period, and the shear spread is negligible ($< 0.4\text{ m s}^{-1}$). The two highlighted members, Ens03 and Ens11, have practically the same shear between $t = 0$ and 36 h, yet Ens03 begins to RI at $t = 31$ h while Ens11 does not.

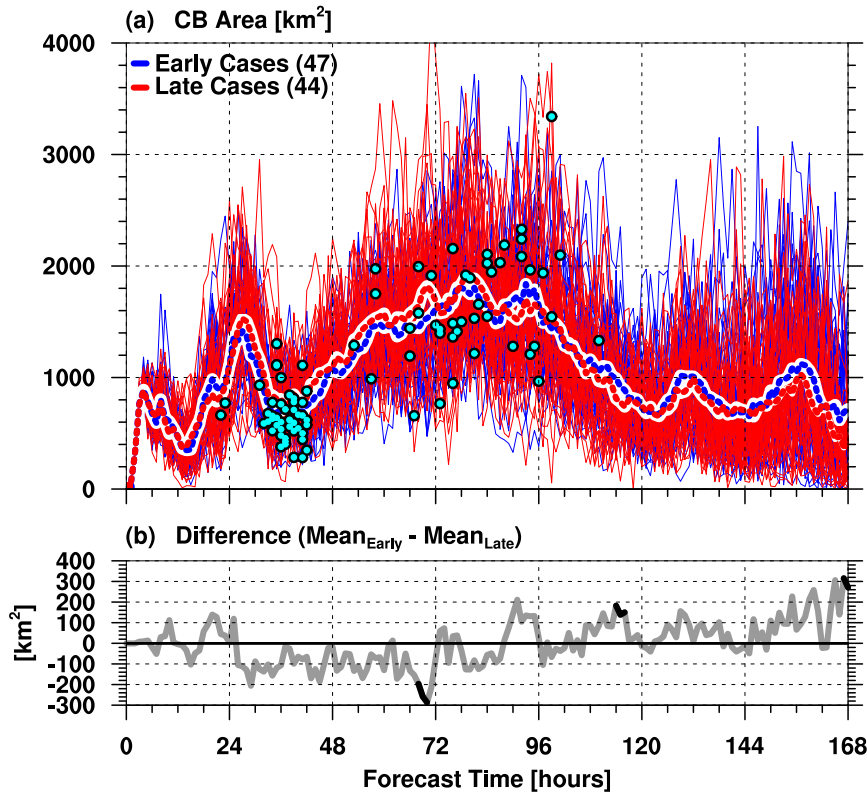


FIG. 8. (a) Ensemble time series of CB activity, expressed as the area covered by CBs within domain 3 ($440 \times 440 \text{ km}^2$). Early cases are in blue, and late cases in red. The thick dashed blue (red) lines denote the means of the early (late) subsets, and the cyan dots indicate RI onset. (b) Difference between the early and late subsets' respective mean CB areas, where statistical significance (95% confidence interval) is highlighted in black.

The histograms in Figs. 11a and 11b summarize the statistical relationship between shear and RI timing in SKEBS-syno and SKEBS-conv. In SKEBS-syno, time-averaged shear magnitude ($t = 24\text{--}48 \text{ h}$) strongly correlates with RI onset time ($r_{pb} = 0.66$; Fig. 11a). This correlation is higher than in the 100-member Grand Ensemble (Fig. 3c), because large-scale perturbations are more effective at driving meaningful differences in wind shear that relate to intensity variations. Although a correlation coefficient of $r_{pb} = 0.51$ suggests a relationship between shear magnitude and RI timing in SKEBS-conv (Fig. 10b), this value is meaningless because the shear differences between the two groups are practically indistinguishable and not statistically significant.

c. Vortex tilt, inner-core inertial stability, and RI

The time series of vortex tilt and inner-core inertial stability from Ens03 and Ens11 of SKEBS-conv in Figs. 10f and 10h indicate that in the absence of environmental variability, RI timing is linked to the structure and vertical coherence of the vortex. Up to $t = 30 \text{ h}$,

the vortex tilt magnitude is similar in Ens03 and Ens11, but thereafter, Ens03 features a substantially smaller vortex tilt (3 vs 15 km; Fig. 10f), allowing it to begin the RI process. The difference in vortex tilt could be related to differences in inertial stability, which begin to emerge by $t = 24 \text{ h}$ (Fig. 10h). The higher inertial stability in the inner core of Ens03 may allow this member to withstand the increasing shear, in the sense that the vortex remains vertically coherent despite the increasing upper-level winds. In contrast, Ens11 is not able to build up inertial stability after an initial increase at $t = 18 \text{ h}$, and may be more susceptible to the shear. This relates to a comparatively larger vortex tilt near $t = 30 \text{ h}$, precluding the member from undergoing RI at this time. (Somewhat surprisingly, the vortex tilt in Ens11 is reduced briefly and the vortex intensifies during $t = 36\text{--}48$ even though the shear increases further.) Note that the separation in inertial stability (Ens03 vs Ens11; Fig. 10h) leads the separation in the maximum wind (Fig. 10b). Both members have the same intensity when member Ens03 begins RI, showing once more that the strength and structure of the wind field are more important than

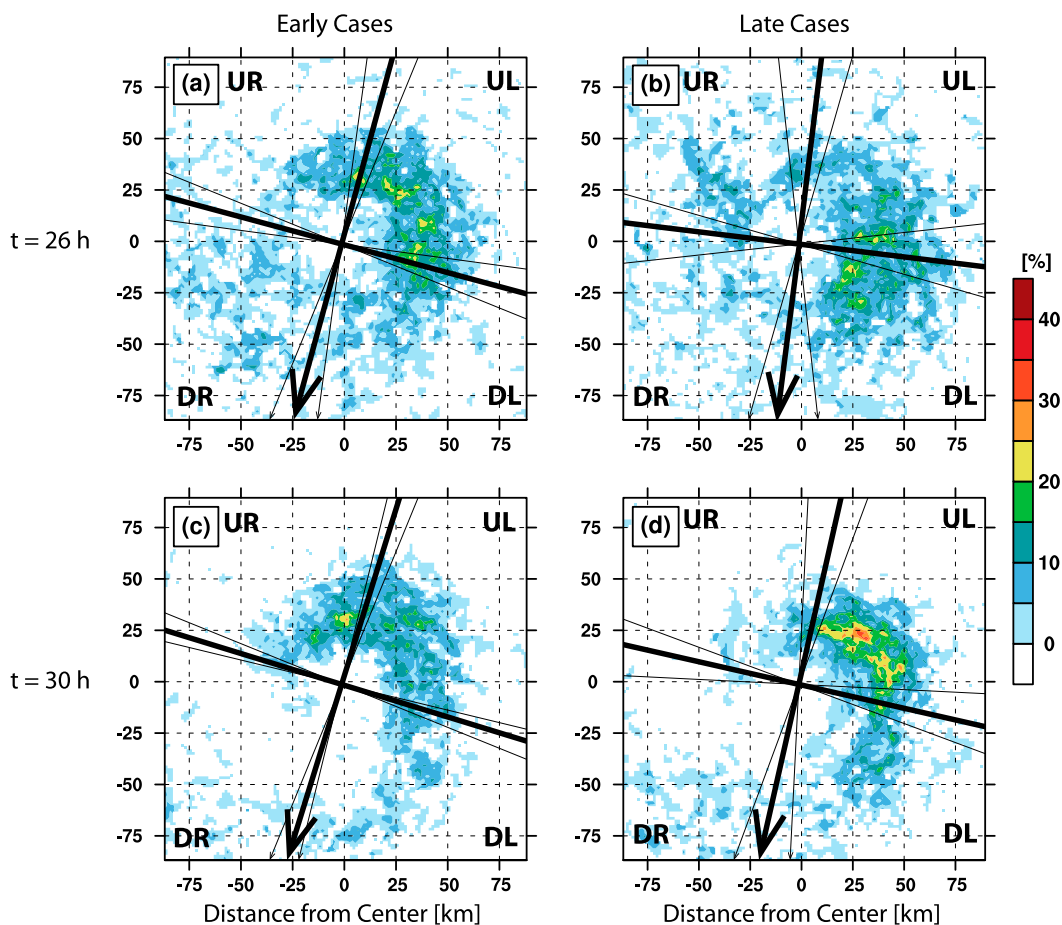


FIG. 9. Horizontal snapshots of CB activity, expressed as the relative frequency of CBs at a given point in the (a),(c) early and (b),(d) late RI cases at $t =$ (a),(b) 26 and (c),(d) 30 h. The thick straight lines are oriented parallel and perpendicular to the average shear vector in the subsets, and divide the plane into the upshear-right (UR), downshear-right (DR), downshear-left (DL) and upshear-left (UL) quadrants. Thin straight lines denote the upper and lower shear direction sextiles, and provide a sense of the shear direction variability (66% of shear vectors lie within the sector spanned by the upper/lower sextiles).

storm intensity. The inertial stability and vortex tilt differences are even larger between Ens03² and Ens02 in SKEBS-syno (Figs. 10e,g), but it is likely that this is a result of environmental differences and not of internal variability alone.

In SKBES-syno, vortex tilt and RI onset are correlated ($r_{pb} = 0.39$), and early RI onset only occurs when the $t = 24$ – 33 averaged vortex tilt is <20 km. The relationship between tilt and RI is even more pronounced in SKEBS-conv (Fig. 11d; $r_{pb} = 0.55$), although the difference in tilt is not statistically significant. The

histograms in Figs. 11e and 11f summarize the relationship between inner-core inertial stability and RI onset time, but again, the differences between the distributions are not statistically significant. In SKEBS-syno, the relationship is ambiguous with a weak negative correlation ($r_{pb} = -0.19$). In contrast, inertial stability and RI onset time in SKEBS-conv exhibit a clearer relationship and show weak-to-moderate correlation ($r_{pb} = -0.41$).

6. TC–environment interactions

The statistical analysis shown in the last two sections reveals that both environmental and internal processes contribute to RI and uncertainty in RI timing. In this section, we provide a more detailed analysis of the previously highlighted members that exemplify the

²There is no correspondence between Ens03 in SKEBS-conv and Ens03 in SKEBS-syno. Both members happened to be the best candidates to highlight the different processes in the respective ensembles.

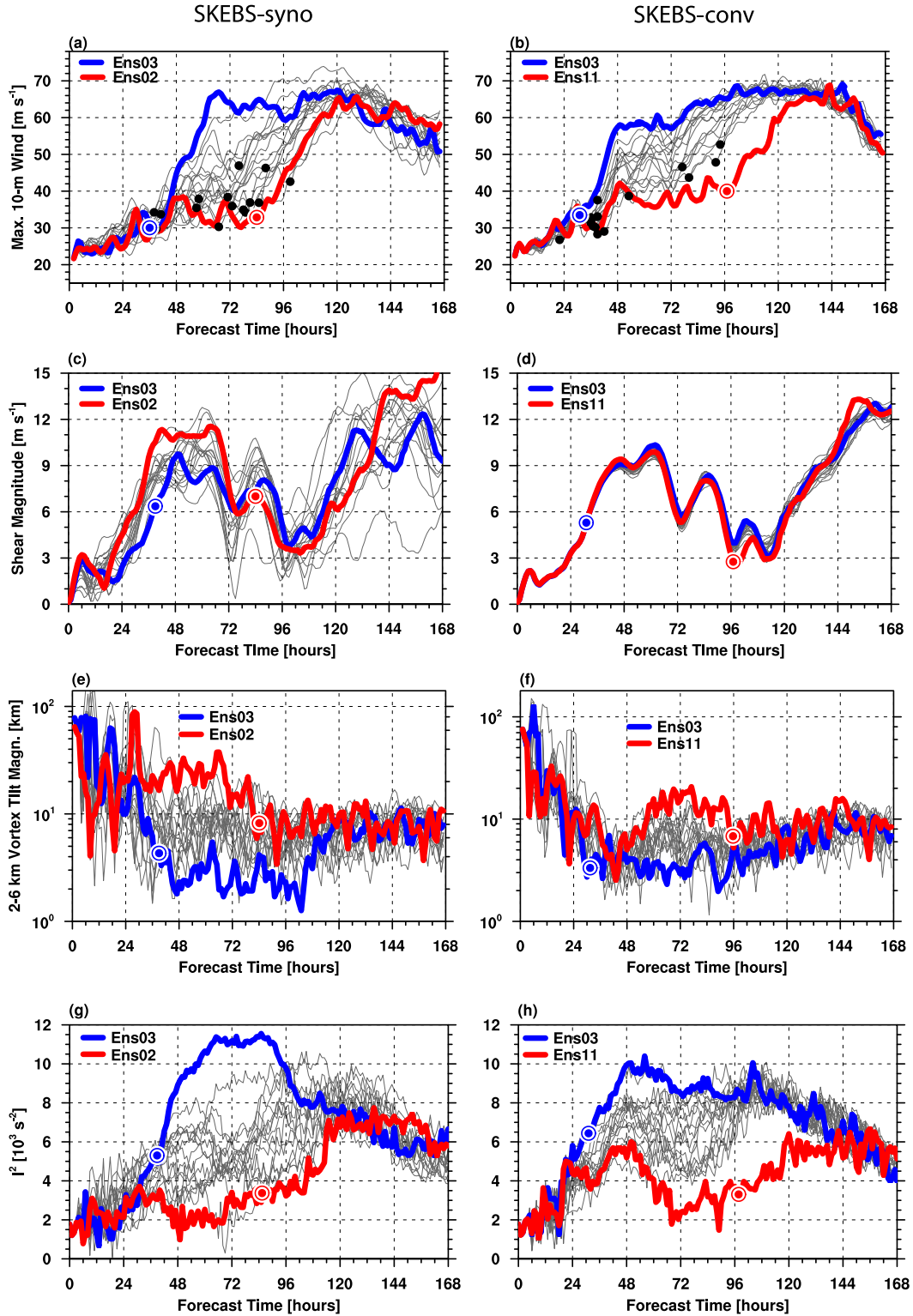


FIG. 10. Maximum 10-m wind speed forecasts from (a) SKEBS-syno and (b) SKEBS-conv. Dots mark RI onset. Shown are the (c),(d) deep-layer wind shear magnitude; (e),(f) vortex tilt magnitude; and (g),(h) $r = 0$ –20-km area-averaged inertial stability at $z = 2$ km. (left) In SKEBS-syno, blue and red highlight a typical early case (Ens02) and a typical late case (Ens03), respectively. (right) In SKEBS-conv, blue and red highlight Ens03 and Ens11, respectively. These four members are further analyzed in Figs. 12–14.

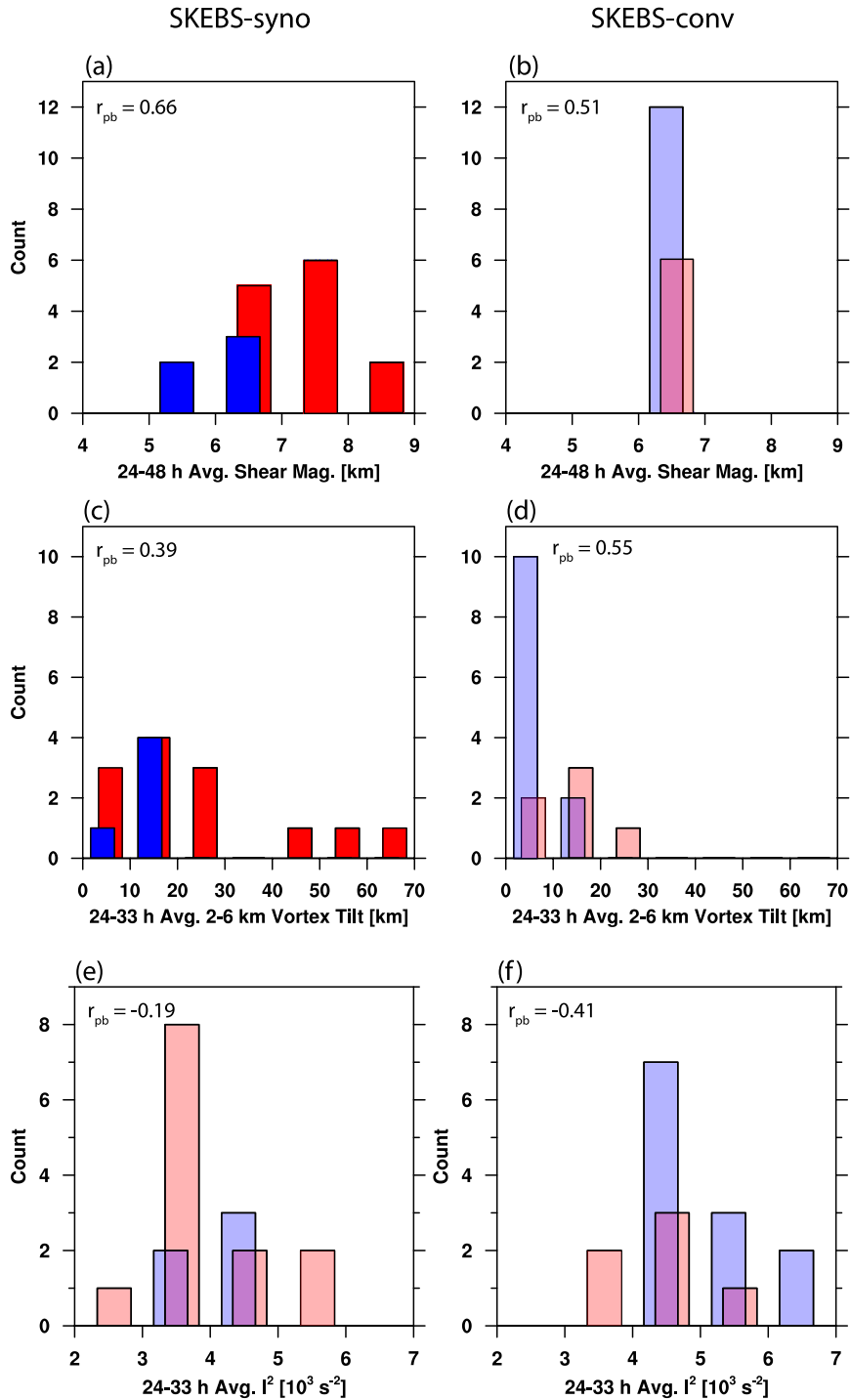


FIG. 11. Histograms of various variables from the (left) SKEBS-syno and (right) SKEBS-conv ensembles. Early and late subsets are in blue and red, respectively, and semitransparent color shading means that the differences between the subsets are not statistically significant at the 95% confidence level. Point-biserial correlation coefficients are plotted in the top-left corners of each panel. (a),(b) The shear magnitude averaged between $t = 24$ and 48 h. (c),(d) The 2–6-km vortex tilt magnitude, time averaged over a 9-h time window ($t = 24$ –33 h) prior to the intensity bifurcation period. (e),(f) The inertial stability, area averaged over a disk with $r = 0$ –20 km at $z = 2$ km and time-averaged between $t = 24$ and 33 h.

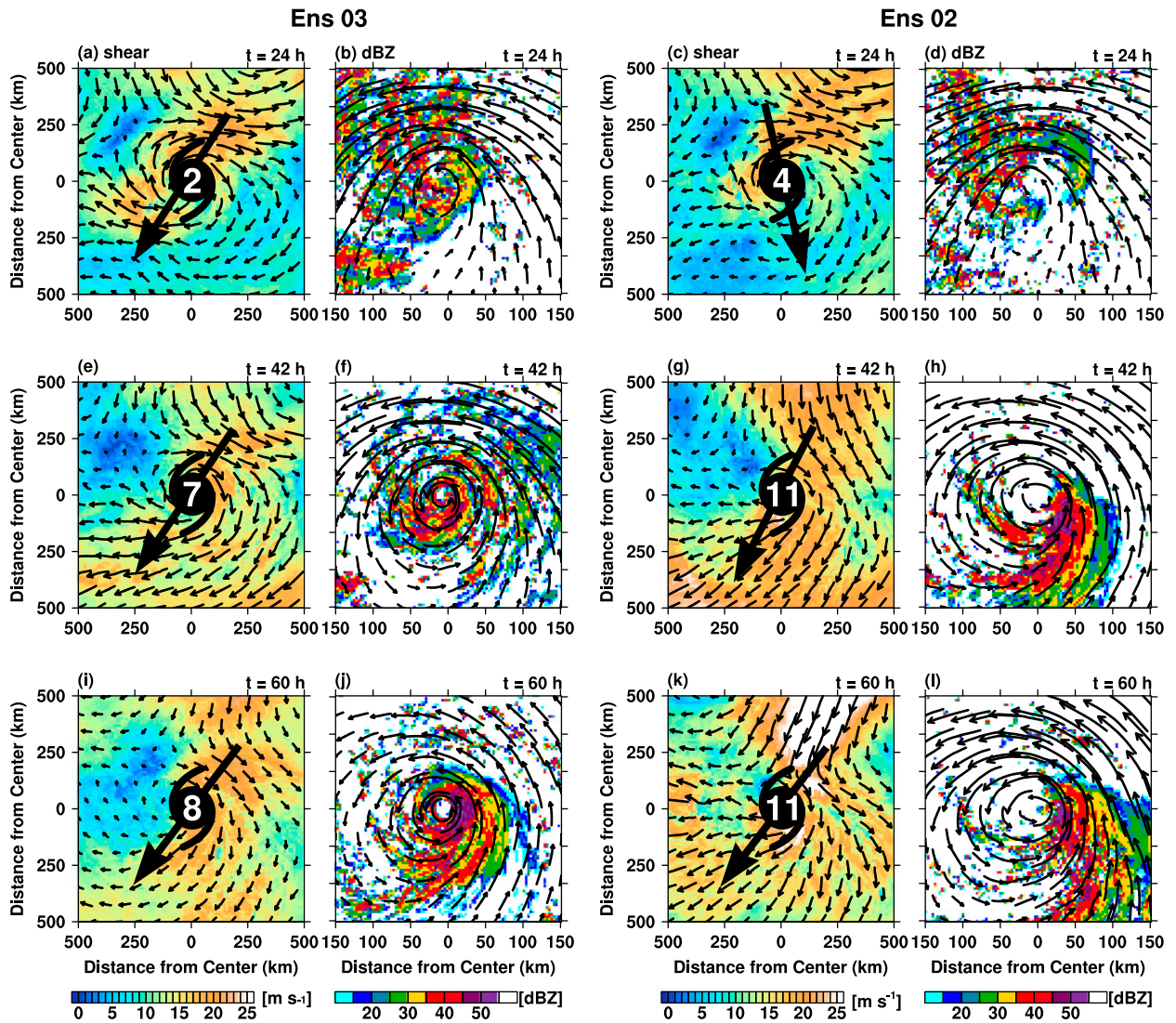


FIG. 12. (left two columns) 200–850-hPa shear and reflectivity at $t =$ (a),(b) 24; (e),(f) 42; and (i),(j) 60 h from SKEBS-syno Ens03. (right two columns) As in (left), but from SKEBS-syno Ens02. The black arrows in the shear plots indicate the shear direction, and the number in the middle of the arrows is the shear magnitude (in m s^{-1}), as computed by the method described in section 4a. See Fig. 10a for the intensity evolution of the two members.

complex interaction between the TCs and their environment.

The differences in shear associated with the outflow of Hurricane Danielle are one of the factors leading to RI timing uncertainty. Members with stronger shear feature more asymmetric vortices, which then struggle to intensify. To illustrate this process, the evolution of the two members with weak and strong shear values from SKEBS-syno is contrasted in Fig. 12. The northerly shear is still comparatively light in both members at $t = 24$ h, although it is already twice as strong in Ens02 (4 m s^{-1} ; Fig. 12c) compared to Ens03 (2 m s^{-1} ; Fig. 12a). The corresponding reflectivity maps of the

strengthening TCs reveal the typical granular precipitation structure of tropical storms that have not yet developed a well-defined eyewall (Figs. 12b,d). Eighteen hours later, the storms have evolved into two very different entities (Figs. 12f,h). The Ens02 case has become a heavily sheared, asymmetric TC with precipitation confined to the downshear-left quadrant, which is typical in sheared TCs (e.g., Chen et al. 2006). The shear is 40% less in Ens03, which has a comparatively more symmetric and better-defined inner core with a closed eyewall (Figs. 12f). Although there are obvious structural differences, the intensity of both members at $t = 42$ h is actually nearly identical

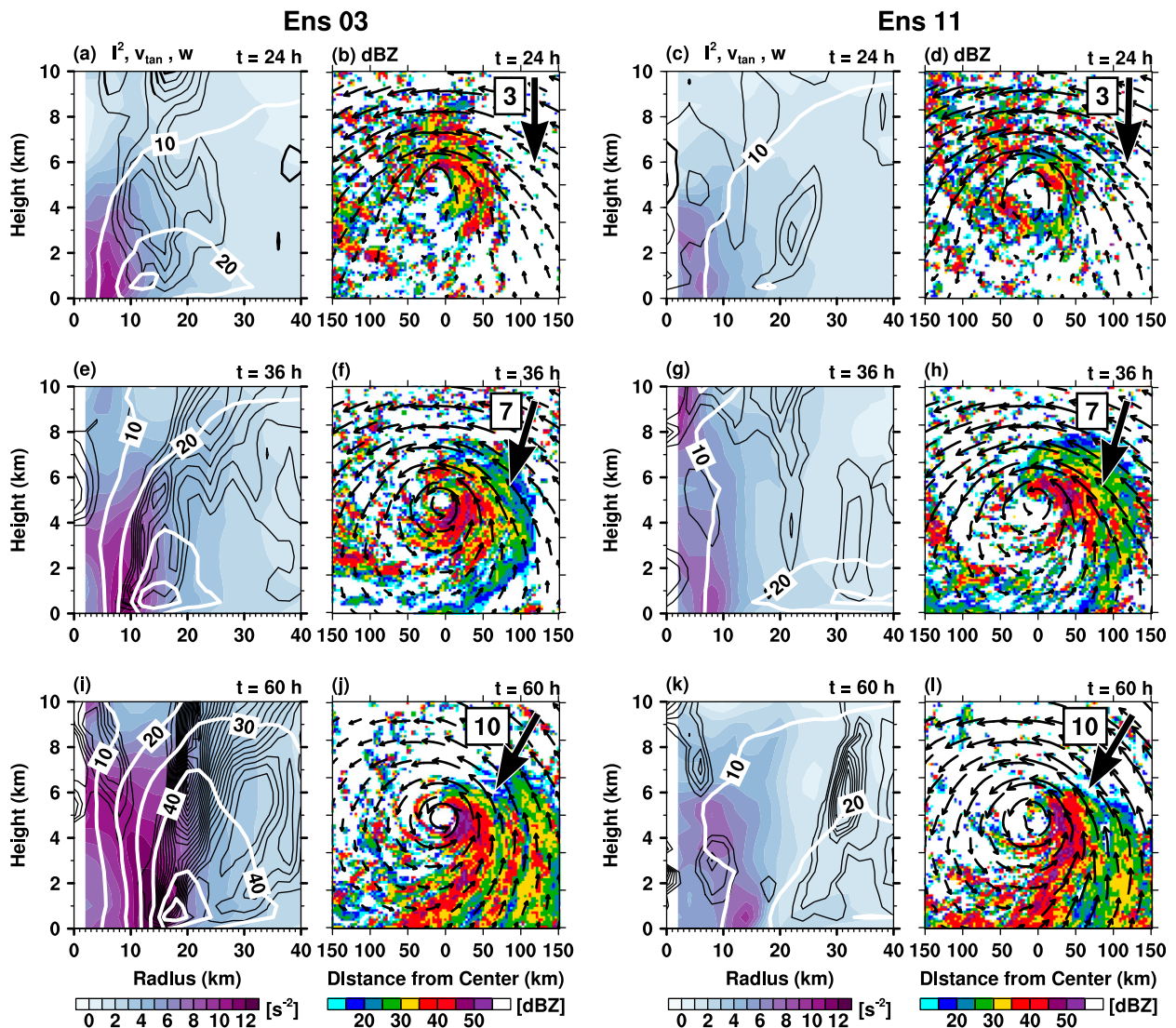


FIG. 13. (left two columns) (a),(e),(i) Radial cross section of inertial stability (purple shading), azimuthally averaged tangential wind (white contours, 10 m s^{-1} interval), and azimuthally averaged vertical velocity (black contours, only values $>0.2 \text{ m s}^{-1}$ are contoured with an interval of 0.2 m s^{-1}). (b),(f),(j) Horizontal cross section of 2-km reflectivity overlaid with horizontal wind vectors at $t =$ (a),(b) 24; (e),(f) 36; and (i),(j) 60 h from SKEBS-conv Ens03. (right two columns) As in (left), but from SKEBS-conv Ens11. The arrows and numbers in the top-right corners of the reflectivity plots denote the shear direction and magnitude (in m s^{-1}), respectively. See Fig. 10b for the intensity evolution of the two members.

(Fig. 10a). By $t = 60 \text{ h}$, Ens03 has intensified into a major hurricane and features a canonical TC core that is nonetheless somewhat asymmetric as a result of 8 m s^{-1} of northeasterly shear (Fig. 12j). In contrast, Ens02 suffers from much stronger shear and retains a highly asymmetric appearance (Figs. 12k,l).

Although RI uncertainty in SKEBS-conv is not associated with shear differences among the ensemble members, the shear does play an indirect role in RI uncertainty. The uncertainty here is intimately linked to how vortices with different inner-core kinematic

structures interact with the environmental shear. In particular, members with higher inertial stability are less susceptible to the detrimental effects of the shear. These members are therefore able to intensify rapidly despite the increasing shear between $t = 24$ and 60 h , as exemplified by the left panels of Fig. 13. At $t = 24 \text{ h}$, Ens03 features a better-defined inner-core structure compared to Ens11 with higher inertial stability inside of $r = 15 \text{ km}$, and a more pronounced vertical velocity and tangential wind maximum (Figs. 13a,c). Note again that the members cannot be distinguished in terms of the peak

wind at this time (Fig. 10b), although the differences in the strength of the azimuthally averaged wind and the vertical extent of the primary circulation reveal that the inner-core structures are quite different. The disparity between the members is in good agreement with the statistical analysis in Fig. 5b, which indicated that a better-defined upper-level circulation correlates with RI onset. The corresponding reflectivity field indicates that Ens03 has a less asymmetric reflectivity signature, especially in its immediate inner core within a few tens of kilometers from the center (Figs. 13b,d). While the shear is still low at this time (magnitude and direction are indicated by the number and arrow in the top-right corners in the reflectivity plots), its effects begin to increase soon after. At $t = 36$ h, Ens03 has intensified despite the increasing shear, whereas Ens11 struggles to establish a well-defined inner core (Figs. 13e–h). By $t = 60$ h, the shear is taking its toll on Ens11. In terms of the kinematic properties, this member’s inner core is now even more disorganized than before, with weaker inertial stability, a broad tangential wind maximum at relatively large radii, and weak, disorganized vertical motion farther away from the center (Fig. 13k). Although the shear is practically the same in Ens03, this member features a classic inner-core structure with well-defined tangential wind and vertical velocity maxima (Fig. 13i). While the differences in the kinematical structure between Ens03 and Ens11 are striking, the asymmetric reflectivity patterns are remarkably similar at this time (Figs. 13 j,l).

One remaining question is what mechanism precipitated the differences in the inner-core structure between Ens03 and Ens11, which have become evident by $t = 24$ h. At first glance, it is difficult to find coherent differences between the two members before this time. This suggests that stochastic processes associated with the interactions between convective features and the vortex-scale circulation play a sizable yet difficult to decipherable role. A series of snapshots of 2-km winds and reflectivity overlaid with vertical velocity contours in Fig. 14 show that there are only subtle differences between the members from $t = 15$ to 21 h. Closer inspection however reveals that at $t = 18$ h Ens03 contains a stronger convective feature to the north of the center (Figs. 14e,f), which is possibly a key player in “forging” the dynamical structure of the inner core. There is some evidence that this particular CB–vortex interaction may be important. For example, the time period shortly after $t = 18$ h marks the beginning of the significant correlation between vortex strength and RI onset (Fig. 5), and coincides with the abrupt increase in inertial stability seen in the early cases after $t = 18$ h (Fig. 7a). The Ens11 case also shows the signature of a CB, but it is not as distinct (Figs. 14g,h). In fact, this burst

exists in one form or another in all members, but because of stochastic effects, the convective features interact differently with the mean vortex in each member. By $t = 24$ h, a reflectivity “hook” resembling a developing eyewall has developed in Ens03 less than 25 km from the center, collocated with a maximum in vertical velocity (Figs. 14m,n). The convective structure in Ens11 is less organized, does not feature an eyewall-like feature, and the vortex is somewhat weaker (Figs. 14o,p). Despite the differences in the organization of convection and the strength of the immediate inner core, there are barely any differences in the area-averaged rainfall and wind speed between Ens03 and Ens11 until $t = 23$ h (Fig. 14q), indicating that the amount of released latent heat and the average vortex strength are similar in both members. Only after $t = 23$ h does the area-averaged rainfall in Ens03 begin to increase at a higher rate compared to Ens11.

The importance of the explicit interactions between convection and the mean vortex with respect to RI timing indicates that RI onset is linked to stochastic processes in SKEBS-conv, in agreement with the idealized study of Zhang and Tao (2013). This finding has important implications for the intrinsic predictability of RI timing and suggests that the stochastic nature of convective processes may make it very difficult to achieve accurate deterministic predictions of RI timing.

7. Distinct dynamical processes in early and late RI cases

The clear separation between the early and late RI cases in terms of RI timing (Fig. 1) suggests that there could be different dynamical processes at play in each of the two groups. The large number of members in each group (47 early and 44 late RI cases) allows for a robust composite analysis. To better compare the characteristics of each groups’ RI period, we present the composites in an RI-relative time framework. The respective intensity evolution of early and late RI cases in the RI-relative frame of reference is shown in Fig. 15. In the 18 h preceding RI onset ($t_{\text{RI}} = -18$ to 0 h), the members in both groups intensify slowly. At the beginning of RI, the early cases are generally of tropical storm/category 1 hurricane intensity (composite mean: 30 m s^{-1} ; Fig. 15a). The late group is more diverse and features TCs ranging from tropical storms to category 3 hurricanes with maximum winds of $>50 \text{ m s}^{-1}$ (composite mean: 40 m s^{-1} ; Fig. 15b). Generally, the early cases intensify at higher rates after RI onset. The mean intensification rate of the early cases during RI is $28 \text{ m s}^{-1} (24 \text{ h})^{-1}$, whereas the mean intensification rate of the late cases is

Ens03

Ens11

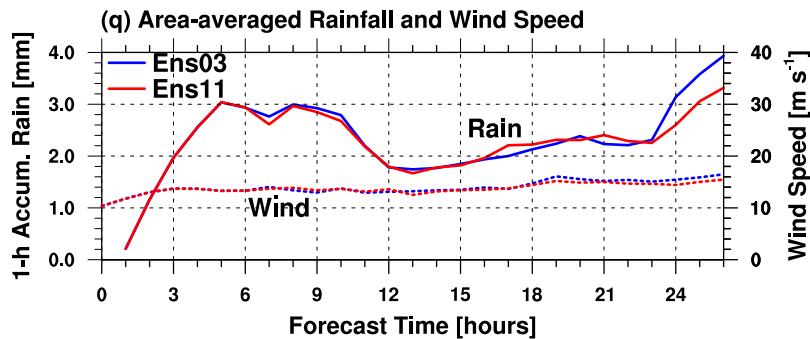
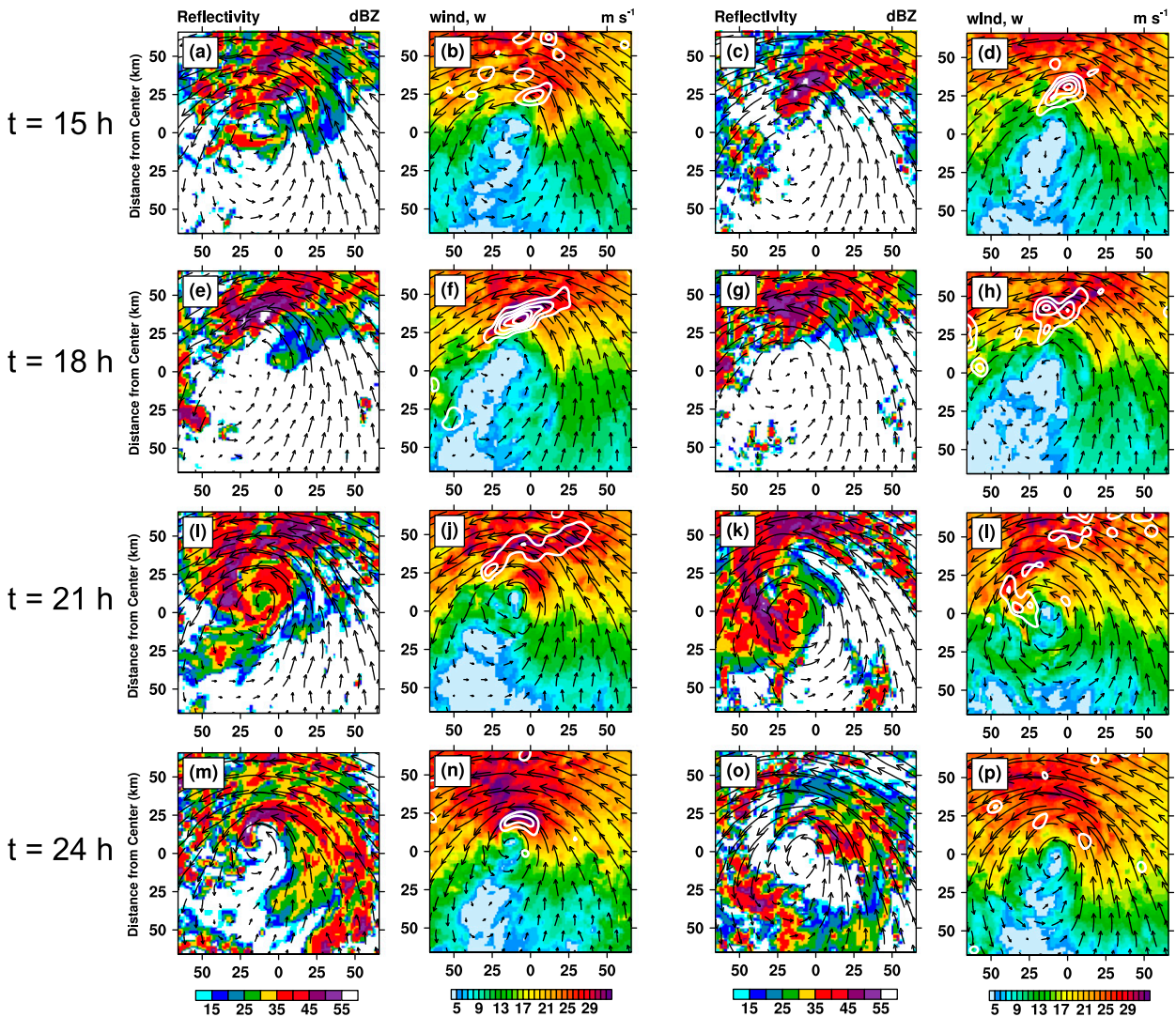


FIG. 14. (left two columns) Cross sections of (a),(e),(i),(m) 2-km reflectivity with horizontal wind vectors, and (b),(f),(j),(n) 2-km wind speed, wind vectors, and vertical velocity (contours at 1 m s⁻¹ intervals from 1 and 5 m s⁻¹) at $t =$ (a),(b) 15; (e),(f) 18; (i),(j) 21; and (m),(n) 24 h from SKEBS-conv Ens03. (right two columns) As in (left), but from SKEBS-conv Ens11. (q) The time series of domain 3 area-averaged wind speed (dashed lines) and 1-h accumulated rainfall (solid lines) from Ens03 (blue) and Ens11 (red).

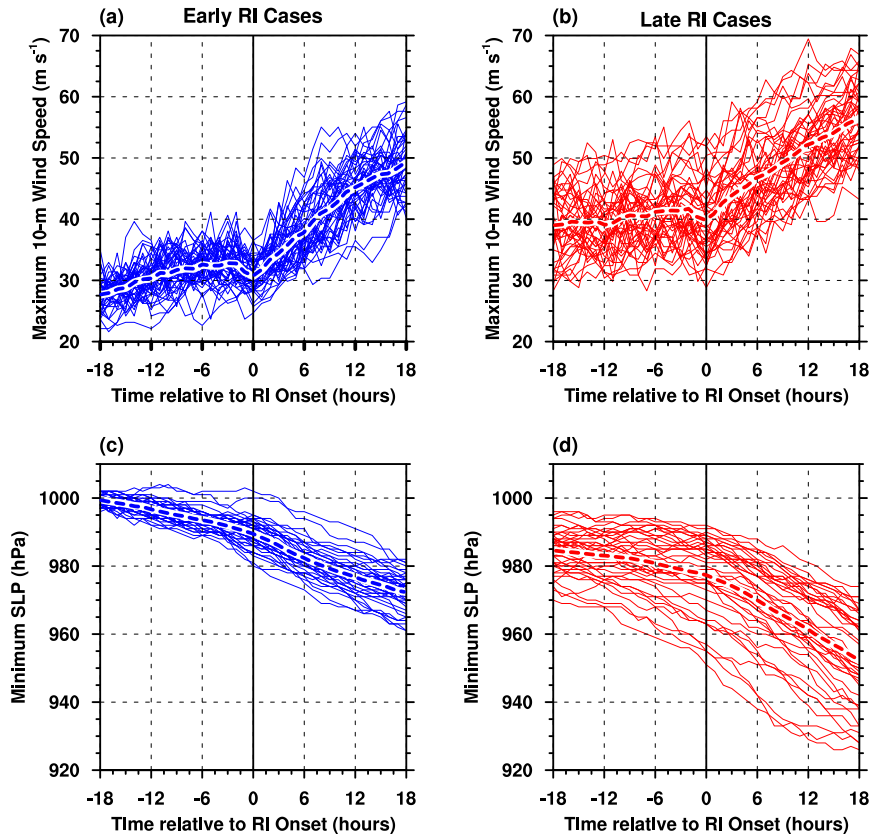


FIG. 15. (a),(b) Maximum wind speed and (c),(d) minimum sea level pressure from the (a),(c) 47 early and (b),(d) 44 late RI cases. Thick dashed lines are the respective averages. Time along the x axis is in hours relative to the RI onset time of each member (t_{RI}).

$23 \text{ m s}^{-1} (24 \text{ h})^{-1}$. Both groups also differ in their rates of minimum SLP deepening prior to and during RI (Figs. 15c,d). In the early group, the change in the deepening rate is barely noticeable, as indicated by the rather linear nature of the lines in Fig. 15c. Conversely, the deepening rate increases after RI onset in the late cases (Fig. 15d; lines bend downward).

a. Evolution of the TC structure

Radius–time Hovmöller diagrams show qualitative differences in vortex structure evolution between the early and late cases during their respective RI periods (Fig. 16). Composites of the $z = 3 \text{ km}$ azimuthally averaged tangential wind speed, reflectivity, and RMW indicate that the RI process in the early cases is associated with the formation of the eyewall (Fig. 16a). The initially flat wind profile develops a well-defined maximum, and a characteristic annulus of reflectivity emerges near $t_{RI} = 0 \text{ h}$. Note that the RMW (black dots) decreases substantially from 50 to 20 km during the 36-h period centered on RI onset (most of the contraction occurs prior to and up to 6 h

after RI onset). In contrast, the RI process in the late group is characterized by a steady amplification of the existing eyewall (Fig. 16b). This behavior is in agreement with Fig. 15, as the late cases are generally more mature and stronger at RI onset. In the late case composite, the RMW only contracts slightly, from 40 to 30 km. This behavior is somewhat inconsistent with the convective ring model of TC intensification (Shapiro and Willoughby 1982; Willoughby et al. 1982), but Stern et al. (2015) showed that intensification does not necessarily coincide with a contraction of the RMW, especially in stronger TCs. The vertical structure of the early cases changed considerably during the RI process, and the initially shallow vortices grew in depth while their mid- to upper-level circulation became established. This is very different from the late cases, which feature deep, well-defined, and vertically coherent vortices reminiscent of mature TCs well before RI onset (not shown).

According to widely accepted paradigms of TC intensification, spinup can be explained by the inward advection of angular momentum (e.g., Ooyama 1969;

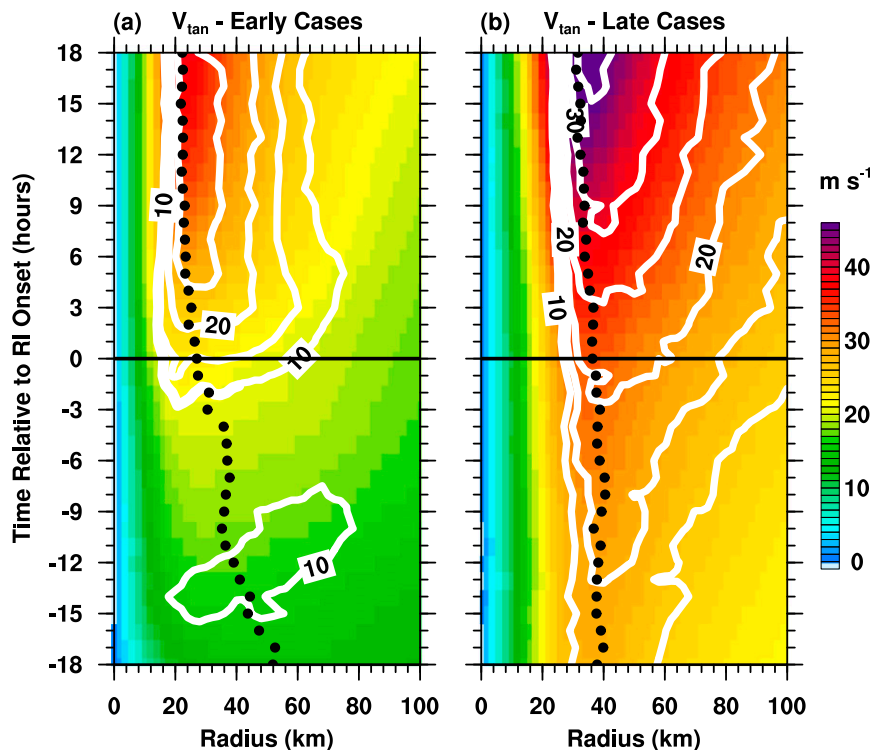


FIG. 16. Time–radius Hovmöller diagrams of azimuthally averaged tangential wind speed (shading, in m s^{-1}), reflectivity (contours, in 5-dBZ intervals starting at 10 dBZ), and RMW (black dots) at $z = 3$ km within an RI-relative framework. Composites of (a) early and (b) late RI cases.

Shapiro and Willoughby 1982; Smith et al. 2009). The early and late cases differ in terms of the radial wind *above* the boundary layer, in the sense that the early cases have a comparatively stronger inflow (Fig. 17).³ Inward-moving angular momentum surfaces match the radial inflow in the early cases (Fig. 17a), whereas in the late cases, the momentum surfaces move inward even at radii without obvious inflow ($r \sim 40\text{--}60$ km; Fig. 17b). This suggests that, in the early cases, inflow above the boundary layer contributes to the inward advection of angular momentum. In the late cases, within the inner region of the TCs, the inflow above the boundary layer does not play a role in bringing angular momentum inward. Future research on this topic can investigate whether the inflow above the boundary layer is actually important for RI in early stage TCs, or whether it is insignificant in light of the comparatively stronger inflow in the frictional boundary layer.

³ We limit our analysis to the inflow above the boundary layer because only here do the subsets show qualitative differences. In terms of the frictional boundary layer inflow, the two groups differ little.

b. Development of the warm core

In a series of recent studies, the development of the upper-level warm core was hypothesized to play an important role in RI (Chen et al. 2011; Zhang and Chen 2012; Chen and Zhang 2013; Chen and Gopalakrishnan 2015). The composites of the temperature anomaly⁴ (averaged between $z = 12\text{--}14$ km) indicate that there are drastic differences in the upper-level thermal structure between the early and late RI cases. While the late case composite in Fig. 18b clearly depicts a developing warm core at the storm center (maximum anomaly ~ 6 K at $t_{\text{RI}} = 18$ h), the signal in the early cases is substantially weaker (maximum anomaly ~ 3 K; Fig. 18a). Note that the bulk of the warming in both cases occurs *after* RI onset, which casts some doubt on the conclusions of Zhang and Chen (2012), who suggest that the warming *causes* RI. Furthermore, the maximum warming in the early cases is not centered at $r = 0$ km, but it coincides with the RMW at the same height.

⁴ Here, the temperature anomaly is the difference between the temperature at a given point and the average temperature within a 200–300-km annulus around the storm center.

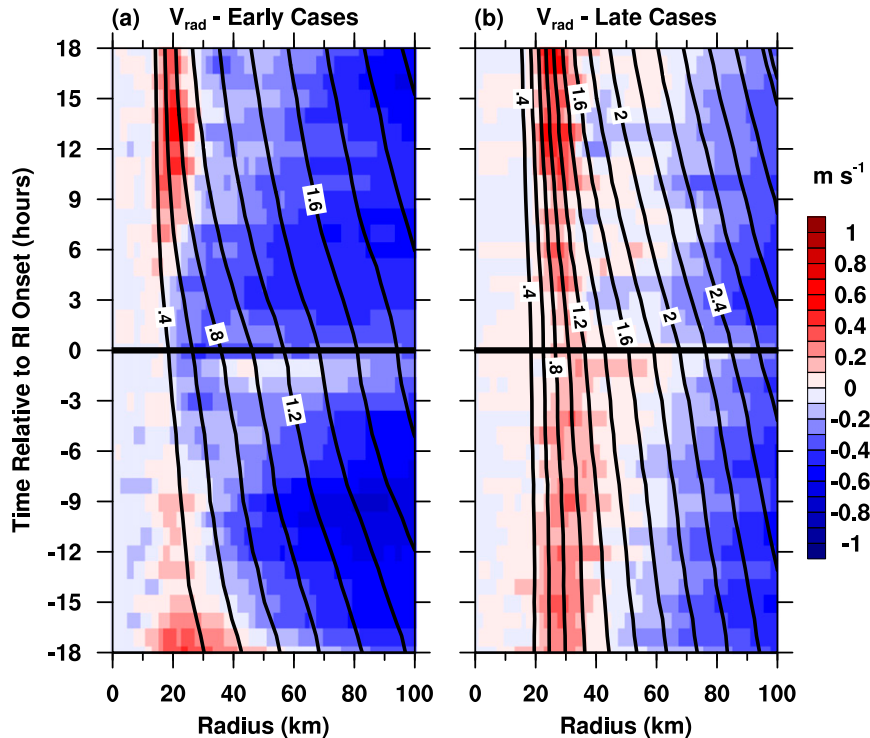


FIG. 17. As in Fig. 16, but for $z = 2$ – 5 -km height-averaged radial velocity (shading, in m s^{-1}) and angular momentum (contours, in $10^6 \text{ m}^2 \text{ s}^{-1}$).

While Fig. 18 depicts the anomaly evolution at upper levels only, the altitude-dependent evolution of the temperature anomaly at the storm center highlights further differences (Fig. 19). The early RI cases are characterized by the development of a warm core at the midlevels (Fig. 19a), whereas the upper-level warm core development during RI is only found in the late case composite (Fig. 19b). Using hydrostatic arguments, Zhang and Chen (2012) showed that upper-level warming is more efficient at lowering the surface pressure, which could explain the increase in the deepening rates in Fig. 15d. In comparison to the downward-bending upper-level isentropes in the late case composite (black contours in Fig. 19b), the midlevel isentropes descend more gradually over a longer period of time. This might result from upper-level and midlevel warming being caused by different physical mechanisms (Stern and Zhang 2013). Note that the late RI cases also feature a midlevel warm anomaly, which starts to develop well before RI. The warming is about the same at the midlevels and upper levels following RI, but the midlevel maximum remains the absolute maximum.

c. Is the upper-level warm core necessary for RI?

In contrast to the warm core studies by Zhang and Chen (2012) and Chen and Zhang (2013), which drew

conclusions from a single model simulation, we examine 100 possible realizations of a TC that displays a wide range of robust characteristics in terms of the relationship between RI and TC structure. While Figs. 18 and 19 showed that there are drastic differences in the warm core development during the respective RI periods of the early and late cases, Fig. 20 suggests that these differences are due to the differences in RI timing. When the entire forecast period is considered, the evolutionary patterns of the temperature anomalies in the early and late RI cases are rather similar. The early cases begin RI before the upper-level warm core appears (Fig. 20a, the period during which RI begins in the 47 early cases is indicated by vertical black lines), while the upper-level warm anomaly begins to develop in *both* groups between $t = 72$ and 96 h, coincident with the RI time window of the late cases (Fig. 20b). Furthermore, a midlevel warm core develops in both groups prior to the upper-level warming, reaching an amplitude of ~ 16 K at $z = 6$ km during the maximum intensity period ($t = 120$ – 144 h). The height of the maximum warming in Fig. 20 is in agreement with Stern and Zhang (2013), but it is unlike the simulations presented in Chen and Zhang (2013) and Ohno and Satoh (2015), which showed a more pronounced warm core near the tropopause. The midlevel warm core is slightly stronger in the early

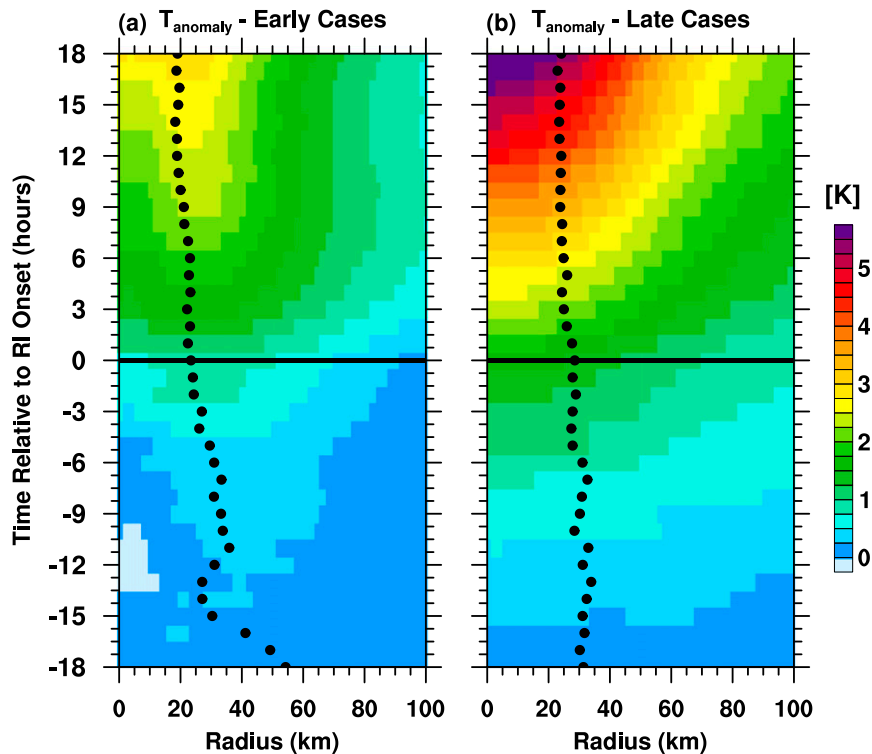


FIG. 18. As in Fig. 16, but for $z = 12\text{--}14\text{-km}$ height-averaged temperature anomaly (shading, in K) and RMW (dots).

group, most likely because the storms in this group are more intense (Fig. 1). Since the temperature anomaly evolution is very similar between the two groups, even though the RI timing is very different, the warm core development does not appear to be a necessary condition for RI. In fact, the ensemble composite analysis reinforces the notion that the warm core is a general

characteristic of mature and strong TCs (Ohno and Satoh 2015).

8. Summary and conclusions

Understanding the physical processes that control the rapid intensification of TCs is paramount for improving

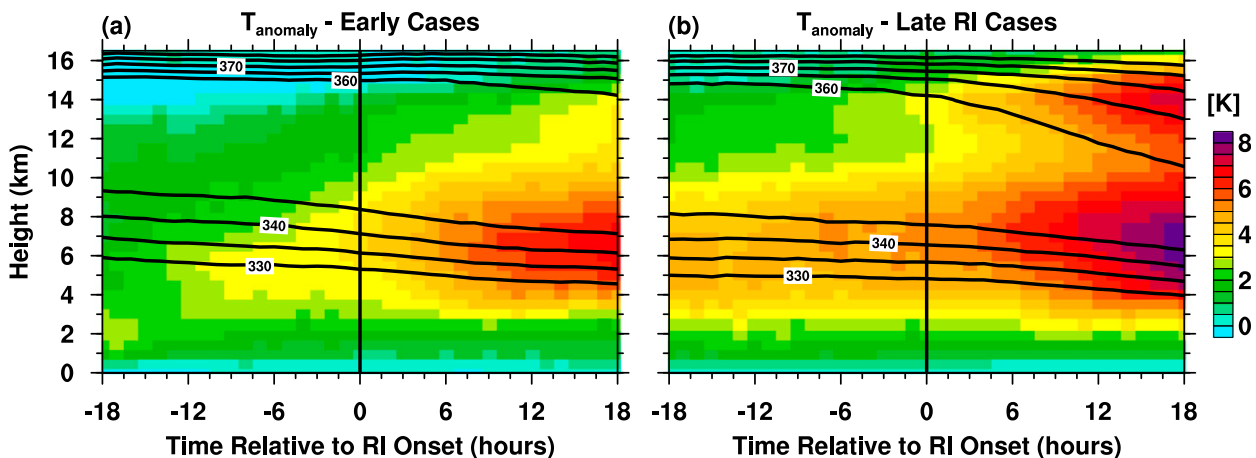


FIG. 19. Time–height composites of the temperature anomaly at the storm center from (a) early and (b) late RI cases (shading), overlaid with potential temperature isotherms from 330 to 345 K and 360 to 380 K (contours, 5-K intervals).

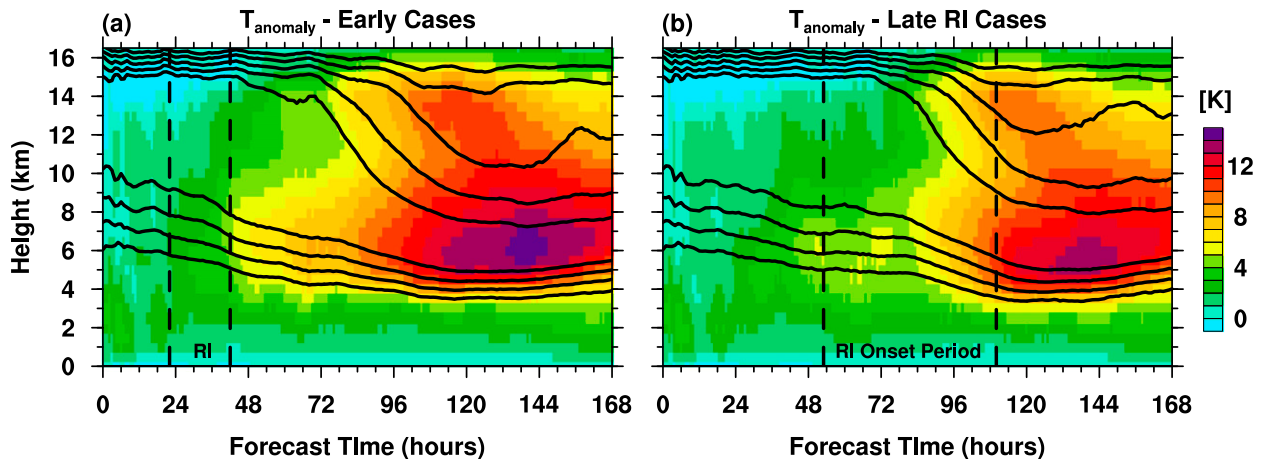


FIG. 20. Time–height diagrams of the temperature anomaly at the storm center (shading, in K). Composites of (a) early and (b) late RI cases. Black contours are the 330–345- and 360–380-K potential temperature isotherms (5-K intervals). Dashed vertical bars delimit the periods during which RI commences in each subset.

the prediction of TC intensity. In this study, we used high-resolution ensembles of Hurricane Earl (2010) created with a stochastic kinetic energy backscatter scheme (SKEBS), which allows for scale-dependent perturbations. A comprehensive analysis of the Grand Ensemble with 100 members provides some insights into the predictability, dynamics, and reasons for uncertainty in RI prediction.

The ensemble generally captured Earl's RI, evidenced by the fact that 91 out of the total of 100 ensemble members qualify as RI cases. Although we cannot say whether this represents the actual probability of Earl undergoing RI, it indicates that the TC environment determines the *overall predictability of RI* in the sense of whether RI will occur. It follows that the predictability of RI is higher if a TC is embedded in an environment that will remain favorable (or unfavorable) for an extended period of time. In contrast, the *timing of RI* seems to have limited predictability, similar to the predictability of TC genesis discussed in Zhang and Sippel (2009). In TCs where the window of opportunity is short, the low predictability of RI timing significantly decreases the overall predictability (in the sense that potential “late cases” would not have a chance to undergo RI).

In terms of the physical mechanisms, we showed that wind shear plays a critical role in the uncertainty of RI timing in two ways. On the one hand, shear variability is directly related to differences in RI timing in the sense that stronger shear leads to a reduction in the likelihood of RI. On the other hand, interactions between the environmental shear, the TC vortex, and convection are responsible for RI timing uncertainty, even when the shear magnitude is uniform within an ensemble. A smaller vortex tilt and a better-defined vertical structure were fair indicators for whether a

member would undergo RI early. Inertial stability can make the vortex resilient to moderate-to-strong shear and allow for RI in an otherwise not ideal environment. These complex feedbacks between convection and the mean vortex imply that the predictability of RI is ultimately limited as a result of the short predictability of convective processes (Zhang and Sippel 2009; Zhang and Tao 2013; JCB16). A manifestation of limited RI predictability is the loss of predictive skill in the SKEBS Grand Ensemble during RI (Judt and Chen 2015).

In contrast to the substantial intensity spread during the intensification period, the maximum intensity reached by most ensemble members is markedly less uncertain. This difference suggests that the intensification and the maximum intensity of TCs are governed by different processes in terms of their dynamics and uncertainty propagation. The contrast between environmental and internal controls implies that maximum intensity predictions for long-lived hurricanes are inherently easier than intensity forecasts for a TC growing toward maturity.

The discovery of distinct RI-related vortex processes was facilitated by the distinction between “early” and “late” RI cases. The two regimes showed differences in the dynamical and thermodynamical structure before, during, and after the RI process, demonstrating that RI is not associated with one particular mechanism. The different processes associated with RI are dependent on the TC's stage in its life cycle. For example, upper-level warming and a more pronounced drop in SLP are exclusively associated with the late RI regime, indicating that the warm core is likely not the immediate cause of RI. Rather, the warming is a general property of strong TCs.

Based on the statistical analysis in Kaplan et al. (2010), RI is more frequent in TCs of tropical storm and low-end hurricane intensity, which implies that the early RI regime is more common in nature (“early” here does not necessarily correspond to an absolute time frame, but rather means that the TCs are of weak intensity at RI onset). RI cases that follow the characteristics of the late regime seem to occur less frequently, although there are some notable examples that involve very intense TCs with large eyes, such as Hurricane Katrina of 2005.

To summarize the results of this study, we present a list of the most important findings below.

- 1) The environment controls the overall tendency for RI and sets the bounds for the maximum TC intensity. The likelihood of RI may be predictable with numerical models as long as the synoptic-scale environment is predictable.
- 2) The initiation of the RI itself has a stochastic component, and the exact timing of RI is controlled by complex interactions between the TC environment (e.g., vertical wind shear), the mean vortex, and convective processes. While the predictability limit of the mean vortex can be >7 days in long-lasting TCs, small-scale convective processes have predictability limits of <12 h (JCB16).
- 3) Two distinct dynamic modes of RI were identified: (i) When RI occurs during the early stages of the TC life cycle, it is generally characterized by a rapidly contracting RMW and the formation of an eyewall. (ii) In mature, well-developed TCs, RI is accompanied by the development of an upper-level warm core, whereas eyewall contraction is less pronounced.

In closing, this study has shown that RI prediction is a complex issue. The relatively short intrinsic predictability of RI timing makes deterministic RI forecasts elusive, and probabilistic predictions based on ensemble forecasts may be the best approach to the operational RI prediction problem. Currently, a statistical model is used operationally that provides probabilistic RI forecasts with limited skill (Kaplan et al. 2010). The questions of whether a potential RI event will be dominated by either large- or small-scale processes or a combination of both could not be answered herein and should be investigated in future studies using a greater number of RI cases.

One of the conclusions of this study is that RI prediction can be improved by reducing environmental uncertainty. Furthermore, advances in data assimilation should be directed toward improving the model representation of the mean vortex structure. The modeling community should invest in improving the parameterization of physical processes (e.g., microphysics, boundary layer turbulence, air–sea momentum/heat exchange).

This may help to reduce some of the gross model biases that still plague the operational models (e.g., Tallapragada et al. 2014) and likely constitute a major source of uncertainty in predicting RI. In fact, model biases tend to nullify advances in improving the initial conditions through data assimilation (Vukicevic et al. 2013).

Acknowledgments. We thank Dr. Judith Berner and Kate Fossell (NCAR) for implementing SKEBS in the WRF Model. Dr. Jason Sippel (NOAA/EMC) and two anonymous reviewers helped improve this manuscript significantly. This research was made possible in part by a grant from The Gulf of Mexico Research Initiative, and by research grants from ONR (N0001401010162) and NASA (NNX14AM78G). Data are publicly available online through the Gulf of Mexico Research Initiative Information and Data Cooperative (GRIIDC; <https://data.gulfresearchinitiative.org>; doi: 10.7266/N7KW5CX6).

REFERENCES

- Berner, J., G. J. Shutts, M. Leutbecher, and T. N. Palmer, 2009: A spectral stochastic kinetic energy backscatter scheme and its impact on flow-dependent predictability in the ECMWF Ensemble Prediction System. *J. Atmos. Sci.*, **66**, 603–626, doi:10.1175/2008JAS2677.1.
- , S.-Y. Ha, J. P. Hacker, A. Fournier, and C. Snyder, 2011: Model uncertainty in a mesoscale ensemble prediction system: Stochastic versus multiphysics representations. *Mon. Wea. Rev.*, **139**, 1972–1995, doi:10.1175/2010MWR3595.1.
- Bosart, L. F., C. S. Velden, W. E. Bracken, J. Molinari, and P. G. Black, 2000: Environmental influences on the rapid intensification of Hurricane Opal (1995) over the Gulf of Mexico. *Mon. Wea. Rev.*, **128**, 322–352, doi:10.1175/1520-0493(2000)128<0322:EIOTRI>2.0.CO;2.
- Braun, S. A., and Coauthors, 2013: NASA’s Genesis and Rapid Intensification Processes (GRIP) field experiment. *Bull. Amer. Meteor. Soc.*, **94**, 345–363, doi:10.1175/BAMS-D-11-00232.1.
- Bui, H. H., R. K. Smith, M. T. Montgomery, and J. Peng, 2009: Balanced and unbalanced aspects of tropical cyclone intensification. *Quart. J. Roy. Meteor. Soc.*, **135**, 1715–1731, doi:10.1002/qj.502.
- Cangialosi, J. P., and J. L. Franklin, 2014: 2013 National Hurricane Center verification report. NHC, 84 pp. [Available online at http://www.nhc.noaa.gov/verification/pdfs/Verification_2013.pdf.]
- Chen, H., and D.-L. Zhang, 2013: On the rapid intensification of Hurricane Wilma (2005). Part II: Convective bursts and the upper-level warm core. *J. Atmos. Sci.*, **70**, 146–162, doi:10.1175/JAS-D-12-062.1.
- , and S. G. Gopalakrishnan, 2015: A study on the asymmetric rapid intensification of Hurricane Earl (2010) using the HWRF system. *J. Atmos. Sci.*, **72**, 531–550, doi:10.1175/JAS-D-14-0097.1.
- , D.-L. Zhang, J. Carton, and R. Atlas, 2011: On the rapid intensification of Hurricane Wilma (2005). Part I: Model prediction and structural changes. *Wea. Forecasting*, **26**, 885–901, doi:10.1175/WAF-D-11-00001.1.

- Chen, S. S., J. Knaff, and F. Marks, 2006: Effects of vertical wind shear and storm motion on tropical cyclone rainfall asymmetries deduced from TRMM. *Mon. Wea. Rev.*, **134**, 3190–3208, doi:10.1175/MWR3245.1.
- , W. Zhao, M. A. Donelan, and H. L. Tolman, 2013: Directional wind–wave coupling in fully coupled atmosphere–wave–ocean models: Results from CBLAST-Hurricane. *J. Atmos. Sci.*, **70**, 3198–3215, doi:10.1175/JAS-D-12-0157.1.
- DeMaria, M., and J. Kaplan, 1994: Sea surface temperature and the maximum intensity of Atlantic tropical cyclones. *J. Climate*, **7**, 1324–1334, doi:10.1175/1520-0442(1994)007<1324:SSTATM>2.0.CO;2.
- Emanuel, K. A., 1986: An air–sea interaction theory for tropical cyclones. Part I: Steady-state maintenance. *J. Atmos. Sci.*, **43**, 585–605, doi:10.1175/1520-0469(1986)043<0585:AASITF>2.0.CO;2.
- , 1988: The maximum intensity of hurricanes. *J. Atmos. Sci.*, **45**, 1143–1155, doi:10.1175/1520-0469(1988)045<1143:TMIOH>2.0.CO;2.
- Guimond, S. R., G. M. Heymsfield, and F. J. Turk, 2010: Multiscale observations of Hurricane Dennis (2005): The effects of hot towers on rapid intensification. *J. Atmos. Sci.*, **67**, 633–654, doi:10.1175/2009JAS3119.1.
- Hendricks, E. A., M. T. Montgomery, and C. A. Davis, 2004: The role of “vortical” hot towers in the formation of Tropical Cyclone Diana (1984). *J. Atmos. Sci.*, **61**, 1209–1232, doi:10.1175/1520-0469(2004)061<1209:TROVHT>2.0.CO;2.
- , M. S. Peng, B. Fu, and T. Li, 2010: Quantifying environmental control on tropical cyclone intensity change. *Mon. Wea. Rev.*, **138**, 3243–3271, doi:10.1175/2010MWR3185.1.
- Hong, X., S. W. Chang, S. Raman, L. K. Shay, and R. Hodur, 2000: The interaction between Hurricane Opal (1995) and a warm core ring in the Gulf of Mexico. *Mon. Wea. Rev.*, **128**, 1347–1365, doi:10.1175/1520-0493(2000)128<1347:TIBHOA>2.0.CO;2.
- Jiang, H., 2012: The relationship between tropical cyclone intensity change and the strength of inner-core convection. *Mon. Wea. Rev.*, **140**, 1164–1176, doi:10.1175/MWR-D-11-00134.1.
- Judt, F., and S. S. Chen, 2015: A new aircraft hurricane wind climatology and applications in assessing the predictive skill of tropical cyclone intensity using high-resolution ensemble forecasts. *Geophys. Res. Lett.*, **42**, 6043–6050, doi:10.1002/2015GL064609.
- , —, and J. Berner, 2016: Predictability of tropical cyclone intensity: Scale-dependent forecast error growth in high-resolution stochastic kinetic-energy backscatter ensembles. *Quart. J. Roy. Meteor. Soc.*, **142**, 43–57, doi:10.1002/qj.2626.
- Kaplan, J., and M. DeMaria, 2003: Large-scale characteristics of rapidly intensifying tropical cyclones in the North Atlantic basin. *Wea. Forecasting*, **18**, 1093–1108, doi:10.1175/1520-0434(2003)018<1093:LCORIT>2.0.CO;2.
- , —, and J. a. Knaff, 2010: A revised tropical cyclone rapid intensification index for the Atlantic and eastern North Pacific basins. *Wea. Forecasting*, **25**, 220–241, doi:10.1175/2009WAF2222280.1.
- Kieper, M. E., and H. Jiang, 2012: Predicting tropical cyclone rapid intensification using the 37 GHz ring pattern identified from passive microwave measurements. *Geophys. Res. Lett.*, **39**, L13804, doi:10.1029/2012GL052115.
- Kossin, J., and M. Eastin, 2001: Two distinct regimes in the kinematic and thermodynamic structure of the hurricane eye and eyewall. *J. Atmos. Sci.*, **58**, 1079–1090, doi:10.1175/1520-0469(2001)058<1079:TDRITK>2.0.CO;2.
- Lee, C.-Y., and S. S. Chen, 2012: Symmetric and asymmetric structures of hurricane boundary layer in coupled atmosphere–wave–ocean models and observations. *J. Atmos. Sci.*, **69**, 3576–3594, doi:10.1175/JAS-D-12-046.1.
- Nguyen, L. T., and J. Molinari, 2012: Rapid intensification of a sheared, fast-moving hurricane over the Gulf Stream. *Mon. Wea. Rev.*, **140**, 3361–3378, doi:10.1175/MWR-D-11-00293.1.
- Nolan, D. S., Y. Moon, and D. P. Stern, 2007: Tropical cyclone intensification from asymmetric convection: Energetics and efficiency. *J. Atmos. Sci.*, **64**, 3377–3405, doi:10.1175/JAS3988.1.
- Ohno, T., and M. Satoh, 2015: On the warm core of a tropical cyclone formed near the tropopause. *J. Atmos. Sci.*, **72**, 551–571, doi:10.1175/JAS-D-14-0078.1.
- Ooyama, K., 1969: Numerical simulation of the life cycle of tropical cyclones. *J. Atmos. Sci.*, **26**, 3–40, doi:10.1175/1520-0469(1969)026<0003:NSOTLC>2.0.CO;2.
- , 1982: Conceptual evolution of the theory and modeling of the tropical cyclone. *J. Meteor. Soc. Japan*, **60**, 369–380.
- Pendergrass, A. P., and H. E. Willoughby, 2009: Diabatically induced secondary flows in tropical cyclones. Part I: Quasi-steady forcing. *Mon. Wea. Rev.*, **137**, 805–821, doi:10.1175/2008MWR2657.1.
- Reasor, P. D., M. D. Eastin, and J. F. Gamache, 2009: Rapidly intensifying Hurricane Guillermo (1997). Part I: Low-wavenumber structure and evolution. *Mon. Wea. Rev.*, **137**, 603–631, doi:10.1175/2008MWR2487.1.
- Rogers, R., 2010: Convective-scale structure and evolution during a high-resolution simulation of tropical cyclone rapid intensification. *J. Atmos. Sci.*, **67**, 44–70, doi:10.1175/2009JAS3122.1.
- , P. Reasor, and S. Lorsolo, 2013: Airborne Doppler observations of the inner-core structural differences between intensifying and steady-state tropical cyclones. *Mon. Wea. Rev.*, **141**, 2970–2991, doi:10.1175/MWR-D-12-00357.1.
- , —, and J. A. Zhang, 2015: Multiscale structure and evolution of Hurricane Earl (2010) during rapid intensification. *Mon. Wea. Rev.*, **143**, 536–562, doi:10.1175/MWR-D-14-00175.1.
- Schubert, W., and J. Hack, 1982: Inertial stability and tropical cyclone development. *J. Atmos. Sci.*, **39**, 1687–1697, doi:10.1175/1520-0469(1982)039<1687:ISATCD>2.0.CO;2.
- Shapiro, L. J., and H. E. Willoughby, 1982: The response of balanced hurricanes to local sources of heat and momentum. *J. Atmos. Sci.*, **39**, 378–394, doi:10.1175/1520-0469(1982)039<0378:TROBHT>2.0.CO;2.
- Shieh, O. H., M. Fiorino, M. E. Kucas, and B. Wang, 2013: Extreme rapid intensification of Typhoon Vicente (2012) in the South China Sea. *Wea. Forecasting*, **28**, 1578–1587, doi:10.1175/WAF-D-13-00076.1.
- Shutts, G., 2005: A kinetic energy backscatter algorithm for use in ensemble prediction systems. *Quart. J. Roy. Meteor. Soc.*, **131**, 3079–3102, doi:10.1256/qj.04.106.
- Skamarock, W. C., and Coauthors, 2008: A description of the Advanced Research WRF version 3. NCAR Tech. Note NCAR/TN-475+STR, 113 pp., doi:10.5065/D68S4MVH.
- Smith, R. K., M. T. Montgomery, and N. Van Sang, 2009: Tropical cyclone spin-up revisited. *Quart. J. Roy. Meteor. Soc.*, **135**, 1321–1335, doi:10.1002/qj.428.
- Stern, D. P., and F. Zhang, 2013: How does the eye warm? Part I: A potential temperature budget analysis of an idealized tropical cyclone. *J. Atmos. Sci.*, **70**, 73–90, doi:10.1175/JAS-D-11-0329.1.
- , J. L. Vigh, D. S. Nolan, and F. Zhang, 2015: Revisiting the relationship between eyewall contraction and intensification. *J. Atmos. Sci.*, **72**, 1283–1306, doi:10.1175/JAS-D-14-0261.1.

- Stevenson, S. N., K. L. Corbosiero, and J. Molinari, 2014: The convective evolution and rapid intensification of Hurricane Earl (2010). *Mon. Wea. Rev.*, **142**, 4364–4380, doi:[10.1175/MWR-D-14-00078.1](https://doi.org/10.1175/MWR-D-14-00078.1).
- Tallapragada, V., C. Kieu, Y. Kwon, S. Trahan, Q. Liu, Z. Zhang, and I.-H. Kwon, 2014: Evaluation of storm structure from the operational HWRF during 2012 implementation. *Mon. Wea. Rev.*, **142**, 4308–4325, doi:[10.1175/MWR-D-13-00010.1](https://doi.org/10.1175/MWR-D-13-00010.1).
- Tao, D., and F. Zhang, 2014: Effect of environmental shear, sea-surface temperature, and ambient moisture on the formation and predictability of tropical cyclones: An ensemble-mean perspective. *J. Adv. Model. Earth Syst.*, **6**, 384–404, doi:[10.1002/2014MS000314](https://doi.org/10.1002/2014MS000314).
- Thompson, P. D., 1957: Uncertainty of initial state as a factor in the predictability of large scale atmospheric flow patterns. *Tellus*, **9**, 275–295, doi:[10.1111/j.2153-3490.1957.tb01885.x](https://doi.org/10.1111/j.2153-3490.1957.tb01885.x).
- Vigh, J. L., and W. H. Schubert, 2009: Rapid development of the tropical cyclone warm core. *J. Atmos. Sci.*, **66**, 3335–3350, doi:[10.1175/2009JAS3092.1](https://doi.org/10.1175/2009JAS3092.1).
- Vukicevic, T., A. Aksoy, P. Reasor, S. D. Aberson, K. J. Sellwood, and F. Marks, 2013: Joint impact of forecast tendency and state error biases in ensemble Kalman filter data assimilation of inner-core tropical cyclone observations. *Mon. Wea. Rev.*, **141**, 2992–3006, doi:[10.1175/MWR-D-12-00211.1](https://doi.org/10.1175/MWR-D-12-00211.1).
- Willoughby, H. E., J. A. Clos, and M. G. Shoreibah, 1982: Concentric eye walls, secondary wind maxima, and the evolution of the hurricane vortex. *J. Atmos. Sci.*, **39**, 395–411, doi:[10.1175/1520-0469\(1982\)039<0395:CEWSWM>2.0.CO;2](https://doi.org/10.1175/1520-0469(1982)039<0395:CEWSWM>2.0.CO;2).
- Zhang, D.-L., and H. Chen, 2012: Importance of the upper-level warm core in the rapid intensification of a tropical cyclone. *Geophys. Res. Lett.*, **39**, L15706, doi:[10.1029/2012GL052355](https://doi.org/10.1029/2012GL052355).
- Zhang, F., and J. A. Sippel, 2009: Effects of moist convection on hurricane predictability. *J. Atmos. Sci.*, **66**, 1944–1961, doi:[10.1175/2009JAS2824.1](https://doi.org/10.1175/2009JAS2824.1).
- , and D. Tao, 2013: Effects of vertical wind shear on the predictability of tropical cyclones. *J. Atmos. Sci.*, **70**, 975–983, doi:[10.1175/JAS-D-12-0133.1](https://doi.org/10.1175/JAS-D-12-0133.1).